IOWA STATE UNIVERSITY
Digital Repository

2019

Understanding the photophysical properties of methylammonium lead halide perovskites

Daniel J. Freppon
Iowa State University

Follow this and additional works at: https://lib.dr.iastate.edu/etd

Part of the Analytical Chemistry Commons

Understanding the photophysical properties of methylammonium lead halide perovskites

by

Daniel Jefferson Freppon

A thesis submitted to the graduate faculty

in partial fulfillment of the requirements for the degree of

MASTER OF SCIENCE

Major: Analytical Chemistry

Program of Study Committee:
Emily A. Smith, Major Professor
Jacob W. Petrich
Javier Vela-Becerra

The student author, whose presentation of the scholarship herein was approved by the program of study committee, is solely responsible for the content of this thesis. The Graduate College will ensure this thesis is globally accessible and will not permit alterations after a degree is conferred.

Iowa State University

Ames, Iowa

2019

DEDICATION

This thesis is dedicated to my family members and friends whom provided support and constructive conversations through my undergraduate and graduate research careers:

My mom, LuAnn, and step-dad Gary. Daily and weekly calls provided support and uplifting words of encouragement and allowing me to discuss my current work and helping me work through everything with thoughtful guidance.

My dad Jeff. Discussions about research and graduate school provided me with much needed insight, and our discussions about samples and possible next steps led to publications and furthering the research I was pursuing.

My grandmas Betty and grandma Cecelia for always being positive and providing wisdom in many decisions I have made over the years. Writing letters throughout my undergraduate and graduate careers with Grandma Betty helped to keep me grounded. Also, just knowing that someone is always there to answer a call or help is something to not be taken for granted!

Alejandra Londoño-Calderon, for the late nights helping me edit my work and providing encouragement to meet my deadlines. Also, supporting me in my decision to switch to a Masters degree, and helping me look forward.

Thank you to my close friends and colleagues: Scott Matthews, Charles Nyamekye, Brett Boote, Dr. Jon Bobbitt, Deyny Mendivelso, Rochelle Dotas, Daniel Geno, Joeseph Nickerson, Sadie Burkhow, Qiaochu Zhu, Dr. Michael Lesoine, Chamari Wijesooriya, Michael and Brittney Cooke, Nicole Stephens, Dr. David Appy, Avinash Singh, Jingzhe Li, Austin Sympson, Dr. Dipak Mainali, Dr. Neha Arora, David Smith, Michael Franks, and Brett Price. Our frequent communication, and in many cases, aid toward my research and personal goals has been and will be forever appreciated.

To everyone, when I was sick, reminding me that finishing this degree was an option, and whatever I decided would be supported, and finally for reminding me that you would be proud of me no matter what.

TABLE OF CONTENTS

LIST OF FIGURES

Page

LIST OF SCHEMES

LIST OF TABLES

NOMENCLATURE

LED	**Light Emitting Diode**
MA	**Methylammonium**
NIR	**Near Infrared**
PL	**Photoluminescence**
XRD	**X-Ray Diffraction**

ACKNOWLEDGMENTS

ABSTRACT

Photostability is important for current organometal halide perovskites being used as materials in light emitting devices, lasers, quantum dots and solar cells. Illumination from different sources such as the sun, lamps, and lasers can alter the physical and PL stability of nanocrystalline perovskites. This instability can be problematic for the use of perovskite quantum dots as molecular probes and lead to deterioration of perovskite-based solar cells. Here, different synthetic pathways are being analyzed using luminescence microscopy to determine the most stable method(s) for preparing physically and PL λ_{max} stable MA lead halide perovskite nanocrystals. Dimensionality is controlled by capping with octylammonium ligands. Two different precursor ratios are evaluated to determine which provide the highest photostability. It is determined that the 1:1.5:1.5 PbX_2:CH_3NH_3X:$CH_3(CH_2)_7X$ precursor ratio provides the most photo-stable MA lead halide perovskite nanocrystals.

CHAPTER 1. INTRODUCTION – METHYLAMMONIUM LEAD HALIDE PEROVSKITES

1.1 General Introduction

Perovskites are crystalline materials with the general formula ABX_3 where A is a relatively small cation, B is a much larger cation compared to A, and X is an anion which bonds to both, typically at the edge centers.[1] While a majority of the perovskites characterized in literature are all inorganic, containing both inorganic cations and anions, organic-inorganic hybrid perovskites have become highly studied in the past two decades. A common hybrid perovskite is methylammonium (MA) lead iodide ($CH_3NH_3PbI_3$) where $CH_3NH_3^+$ cation is the smaller "A" cation, Pb^{2+} is the larger "B" cation, and I^- is the complementary "X" anion. Bromide and chloride are also used, other than iodide, are common anions used to produce MA lead halide perovskites.

MA lead halide perovskites are currently being investigated in many areas of material science. These materials are being evaluated for light-electricity conversion materials (solar cells),[2,3] LEDs for displays,[4] quantum dots,[5,6] photo-detection,[7,8] and lasing.[9,10] The efficiency and usefulness of perovskite-based devices depend on the mechanical and photo stability of these materials. Illumination from lamp sources (luminescence microscopy) and sunlight (solar cells) has been found to lead to the deterioration of the structural stability of MA lead halide materials leading to poor photostability. Many modifications to the cation, anion, capping material, substrate, or photosensitizer have been investigated in order to improve their photostability.[11-13]

MA lead halide perovskite photo-properties in the visible and near infrared (NIR) can be tuned by incorporating various amounts of Cl, Br, and I anions,[14,15] shown in Fig. 1.1. $CH_3NH_3PbCl_3$ perovskite nanocrystals have the lowest photoluminescence (PL) wavelength

maximum (λ_{max}) near 400 nm. $CH_3NH_3PbBr_3$ perovskite nanocrystals have an intermediate PL λ_{max} near 500 nm. $CH_3NH_3PbI_3$ perovskite nanocrystals have the highest PL λ_{max} near 750 nm. Fig. 1.1 shows the lattice parameter and the absorption edge of each MA lead halide loading in toluene. The x-axis represents the halide precursor (PbX_2) loading, not necessarily the halide incorporation into the crystalline lattice. In chapter 3 of this dissertation, the single nanocrystalline luminescence spectra are collected in the dry state. The solvent, and whether a solvent is used to collect the spectrum, affect the PL λ_{max}.
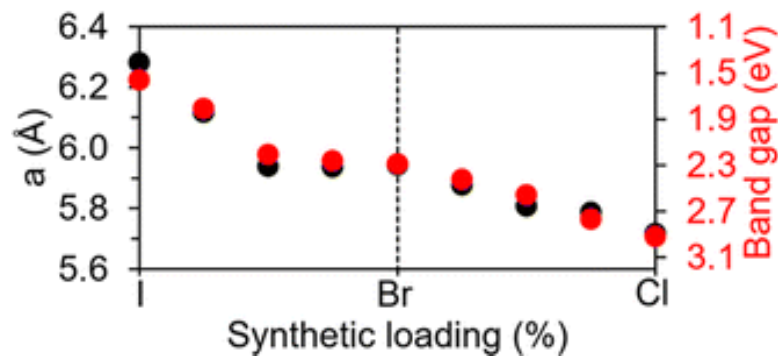
Fig. 1.1. (Black) Lattice parameter over a range of Cl, Br, and I compositions including mixed Cl/Br and Br/I loading. (Red) Adsorption edges of various perovskite nanocrystals over a range of Cl, Br, and I compositions including mixed Cl/Br and Br/I loading. Collected by Dr. Long Men of the Vela group.[16]

1.2 Precursor Effects on Perovskite Nanocrystal Photostability

There are a multitude of synthetic methods to produce perovskite nanocrystals. Two synthetic pathways utilizing different precursor ratios will be discussed: (1) 1:1.5:1.5 PbX_2:CH_3NH_3X:$CH_3(CH_2)_7X$ and (2) 1:3:3 PbX_2:CH_3NH_3X:$CH_3(CH_2)_7X$. Data presented in Chapter 2 suggests a lower precursor ratio of 1:1.5:1.5 produces more photostable perovskites. Other than the precursor ratio, the relative abundance of different halides in the mixed-halide MA lead halide perovskites can affect the photostability of the nanocrystals. Fig. 1.2 shows the stable luminescence λ_{max} of a single $CH_3NH_3PbI_3$ nanocrystal (Fig. 1.2b) and the shift in λ_{max} of

a single mixed $CH_3NH_3Pb(I_{0.8}Br_{0.2})_3$ nanocrystal (Fig. 1.2a). The shift in λ_{max} of the mixed

halide nanocrystal could be due to light-induced phase transformations to I-rich and Br-rich

domains, which are investigated using in-situ x-ray diffraction (XRD) experiments and are

further discussed in Chapter 2.
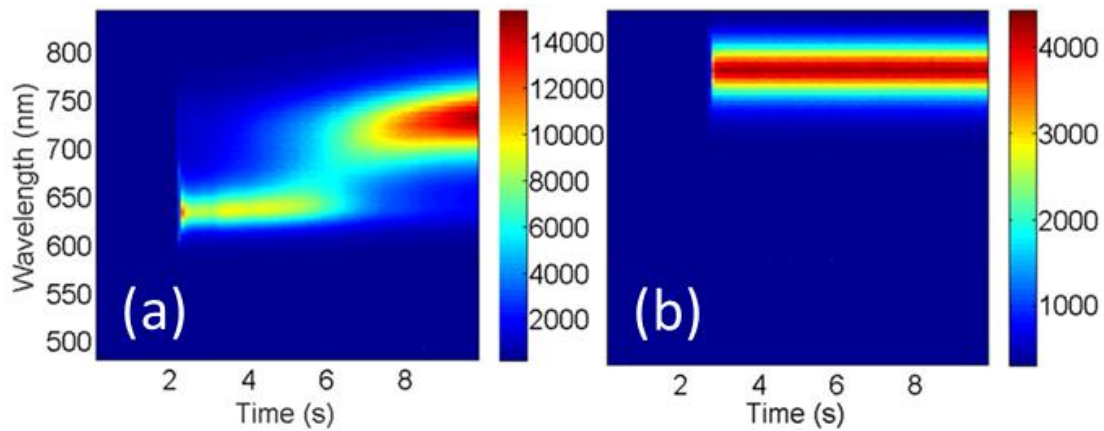
Fig. 1.2. Time correlated luminescence spectra of single (a) $CH_3NH_3Pb(I_{0.8}Br_{0.2})_3$ (80% iodide and 20% bromide loading) and (b) $CH_3NH_3PbI_3$ (100% iodide loading) perovskite nanocrystals. The void for the first 2 seconds corresponds to the off-time of the 532 nm excitation source.

1.3 Blinking Characteristics of Methylammonium Lead Halide Perovskites

Inorganic quantum dots are prone to exhibit luminescence intermittency, or blinking.[17-19]

This phenomenon is represented by periods of luminescence (bright) and non-luminescence

(dark). MA lead halide nanocrystals also exhibit this blinking behavior.[20,21] While blinking can

be advantageous for luminescent molecular probes, allowing for a confirmation that the signal is

generated from one nanocrystal at a specific location, blinking can also be an indicator of the

presence of structural defects. Specifically, surface defects can lead to a blinking behavior in all

inorganic quantum dots.[22] Surface traps lead to non-radiative recombination of electrons and

holes generated upon illumination of nanocrystalline materials. Fig 1.3 represents the

luminescence intensity over time of a single $CH_3NH_3Pb(Br_{0.50}I_{0.50})_3$ nanocrystal which exhibits

luminescence intermittence. Chapter 3 discusses the blinking properties of CH_3NH_3Pb $(Br_{1-x}I_x)_3$ nanocrystals.
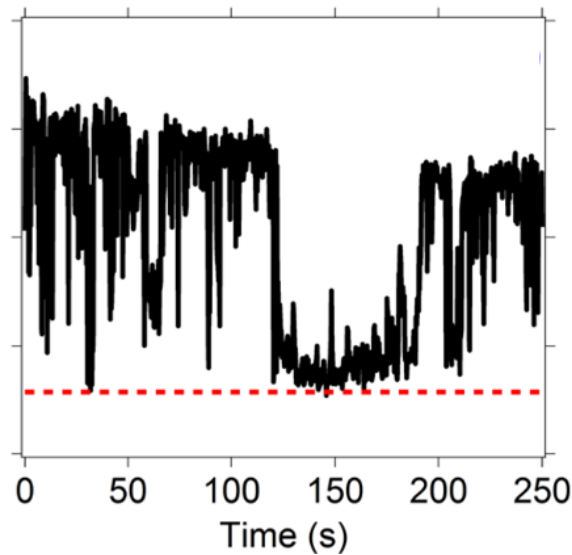
Fig. 1.3. Representative luminescence intensity versus time graphs for a single CH_3NH_3Pb $(Br_{0.50}I_{0.50})_3$ nanocrystal. The dotted red line represents the intensity value which is three standard deviations above the average background signal.

1.4 Phase Transformations under Photoillumination

In order to test the hypothesis of phase transformation of the mixed halide perovskite nanocrystals, a control experiment was conducted under the same experimental in-situ laser illuminated XRD experiments elaborated on in chapter 2. The control analyte was a photoswitchable molecule, trans-azobenzene. Trans-azobenzene undergoes a trans- to cis-isomerization change under laser illumination or under high thermal pressure.[23-25] An observation of a shift in XRD peaks corresponding to a trans- to cis- isomerization in azobenzene is observed. This observation confirms that the in situ laser illumination during XRD collection does provide an environment where photochemical reactions can occur. This result confirms that the shift in λ_{max} of the mixed halide perovskite nanocrystal is not due to a solid-phase I- and Br-domain shift.

1.5 Structure of Thesis

Chapter two discusses the effects of the MA lead halide nanocrystal precursor ratio and the iodide and bromide loading on λ_{max} stability under 1×10^5 W/cm² laser illumination. Chapter three discusses the blinking statistics of the Cl-, Br-, and I-based single MA lead halide nanocrystals. Chapter four discusses the experiments studying the in-situ laser illuminated trans- to cis-azobenzene isomerization. The experiments described in Chapter four show that a shift in the photo-switchable azobenzene molecule during an in-situ XRD experiment, which show that a shift could be observed in the perovskite materials if in fact there was a shift in the XRD spectrum. This work paves the way for measuring phase shifts in situ in perovskite and other materials.

References

(1)   Wolfram, T.; Ellialtioglu, S. *Electronic and optical properties of d-band perovskites*; Cambridge University Press, 2006.

(2)   Snaith, H. J. *The Journal of Physical Chemistry Letters* 2013, *4*, 3623.

(3)   Im, J.-H.; Lee, C.-R.; Lee, J.-W.; Park, S.-W.; Park, N.-G. *Nanoscale* 2011, *3*, 4088.

(4)   Kumawat, N. K.; Dey, A.; Narasimhan, K. L.; Kabra, D. *ACS Photonics* 2015, *2*, 349.

(5)   Park, Y.-S.; Guo, S.; Makarov, N. S.; Klimov, V. I. *ACS Nano* 2015, *9*, 10386.

(6)   Zhang, F.; Zhong, H.; Chen, C.; Wu, X.-g.; Hu, X.; Huang, H.; Han, J.; Zou, B.; Dong, Y. *ACS Nano* 2015, *9*, 4533.

(7)   De Wolf, S.; Holovsky, J.; Moon, S.-J.; Löper, P.; Niesen, B.; Ledinsky, M.; Haug, F.-J.; Yum, J.-H.; Ballif, C. *The Journal of Physical Chemistry Letters* 2014, *5*, 1035.

(8)   Mahshid, A.; Ting, W.; Bin, H. *Advanced Materials* 2017, *29*, 1605242.

(9)   Zhu, H.; Fu, Y.; Meng, F.; Wu, X.; Gong, Z.; Ding, Q.; Gustafsson, M.; Trinh, M.; Jin, S.; Zhu, X. *Nature Materials* 2015, *14*, 636.

(10)   Deschler, F.; Price, M.; Pathak, S.; Klintberg, L. E.; Jarausch, D.-D.; Higler, R.; Hüttner, S.; Leijtens, T.; Stranks, S. D.; Snaith, H. J.; Atatüre, M.; Phillips, R. T.; Friend, R. H. *The Journal of Physical Chemistry Letters* 2014, *5*, 1421.

(11)   Govindhasamy, M.; Soichiro, T.; Gai, M.; Shusaku, K.; Hitoshi, N.; Tomokazu, U.; Hiroshi, I.; Seigo, I. *Japanese Journal of Applied Physics* 2015, *54*, 08KF08.

(12)   Sangni, W.; Furong, H.; Liya, Z.; Jianwu, W.; Youling, X.; Peng, J.; Zhuo, C.; Zuodong, Y.; Qi, P.; Zhong, Z. J. *ChemNanoMat* 2018, *4*, 409.

(13)   Yang, Z.; Feng, W.; Yu, C.; Jian-Pu, W.; Hong-Hua, F.; Antonietta, L. M.; Ni, Z.; Ching-Ping, W. *Advanced Energy Materials* 2017, *7*, 1701048.

(14)   Akkerman, Q. A.; D'Innocenzo, V.; Accornero, S.; Scarpellini, A.; Petrozza, A.; Prato, M.; Manna, L. *Journal of the American Chemical Society* 2015, *137*, 10276.

(15)   Rosales, B. A.; Hanrahan, M. P.; Boote, B. W.; Rossini, A. J.; Smith, E. A.; Vela, J. *ACS Energy Letters* 2017, *2*, 906.

(16)   Rosales, B. A.; Men, L.; Cady, S. D.; Hanrahan, M. P.; Rossini, A. J.; Vela, J. *Chemistry of Materials* 2016, *28*, 6848.

(17)   Barnes, M. D.; Mehta, A.; Thundat, T.; Bhargava, R. N.; Chhabra, V.; Kulkarni, B. *The Journal of Physical Chemistry B* 2000, *104*, 6099.

(18)   Gibson, N. A.; Koscher, B. A.; Alivisatos, A. P.; Leone, S. R. *The Journal of Physical Chemistry C* 2018, *122*, 12106.

(19)   Tian, Y.; Merdasa, A.; Peter, M.; Abdellah, M.; Zheng, K.; Ponseca, C. S.; Pullerits, T.; Yartsev, A.; Sundström, V.; Scheblykin, I. G. *Nano Letters* 2015, *15*, 1603.

(20)   Yuan, H.; Debroye, E.; Caliandro, G.; Janssen, K. P. F.; van Loon, J.; Kirschhock, C. E. A.; Martens, J. A.; Hofkens, J.; Roeffaers, M. B. J. *ACS Omega* 2016, *1*, 148.

(21)   Freppon, D. J.; Men, L.; Burkhow, S. J.; Petrich, J. W.; Vela, J.; Smith, E. A. *Journal of Materials Chemistry C* 2017.

(22)   Lo, S. S.; Major, T. A.; Petchsang, N.; Huang, L.; Kuno, M. K.; Hartland, G. V. *ACS Nano* 2012, *6*, 5274.

(23)   Hartley, G. S. *Journal of the Chemical Society (Resumed)* 1938, 633.

(24)   Fischer, E.; Frankel, M.; Wolovsky, R. *The Journal of Chemical Physics* 1955, *23*, 1367.

(25)   Tsuda, M.; Kuratani, K. *Bulletin of the Chemical Society of Japan* 1964, *37*, 1284.

CHAPTER 2. SYNTHETIC CONTROL OF THE PHOTOLUMINESCENCE STABILITY OF ORGANOLEAD HALIDE PEROVSKITES

Modified from a manuscript published in The Journal of the Mexican Chemical Society (2019); reproduced with permission.

Daniel J. Freppon,[1,2] Long Men,[1,2] Ujjal Bhattacharjee,[1,2] Bryan A. Rosales,[1] Feng Zhu,[1] Jacob W. Petrich,[1,2] Emily A. Smith,*[1,2] Javier Vela*[1,2]

[1]Department of Chemistry, Iowa State University, and [2]Ames Laboratory, Ames, Iowa 50011

*Corresponding Authors email: esmith1@iastate.edu, vela@iastate.edu

Abstract

An optimized synthetic procedure for preparing photostable nanocrystalline methylammonium lead halide materials is reported. The procedure was developed by adjusting the lead halide to methylammonium/octylammonium halide precursor ratio. At a high precursor ratio (1:3), a blue-shifted photoinduced luminescence peak is measured at 642 nm for $CH_3NH_3PbI_3$ with 0.01 to 12 mJ pulsed-laser irradiation. The appearance of this peak is reversible over 300 min upon blocking the irradiation. In order to determine if the peak is the result of a phase change, *in situ* x-ray diffraction measurements were performed. No phase change was measured with an irradiance that causes the appearance of the photoinduced luminescence peak. Luminescence microscpectroscopy measurements showed that the use of a lower precursor ratio (1:1.5) produces $CH_3NH_3PbI_3$ and $CH_3NH_3PbBr_3$ perovskites that are stable over 4 min of illumination. Given the lack of a measured phase change, and the dependence on the precursor ratio, the photoinduced luminesce peak may derive from surface trap states. The enhanced photostability of the resulting perovskite nanocrystals produced with the optimized synthetic procedure supports their use in stable optoelectronic devices.

2.1 Introduction

Organolead halide perovskite semiconductors of general composition $RPbX_3$ (R = organic monocation, such as $CH_3NH_3^+$; X = halide, such as I^- or Br^-) have drawn attention as both photovoltaic[1,2] and optoelectronic[3] materials. Broad light absorption and long carrier diffusion lengths make perovskites ideal light harvesters.[4] The certified power conversion efficiency of perovskite solar cells surged from 3.8% to over 22% in the last 8 years.[5-10] In spite of these many advantages, organometal halide perovskites suffer from instability against moisture, heat and light.[11-13] A deeper understanding of the fundamental physical and chemical behavior of perovskites could help in mitigating these instability issues, thus enabling their implementation and deployment into many energy technologies.[14,15]

Efforts to improve the physical and chemical properties of perovskites have focused primarily on tuning their composition or dimensionality.[16,17] Compositional and dimensional control are useful in tuning the bandgap energies of some perovskite materials.[18,19] Partial substitution with long alkylammonium cations leads to low dimensional perovskites,[20-22] some of which exhibit enhanced moisture stability. Control of optoelectronic properties through mixing cations and halides has been widely exploited in enhancing the power conversion efficiency of perovskite solar cells. Compositional variants of halide perovskites have bandgap and luminescence energies that cover the entire visible spectrum.[9,23-25] Halide substitution also leads to enhanced stability, as $CH_3NH_3PbI_3$ solar cells doped with Br show long-lasting resistance against humidity.[26,27] $CH_3NH_3PbBr_3$ displays lower sensitivity to concentrated sunlight compared to $CH_3NH_3PbI_3$.[22,28]

A few reports describe the unusual photophysical behavior of organometal halide perovskites, specifically a reversible shift in photoluminescence maximum (PL_{max}) under thermal

and photochemical conditions.[29-31] Gottesman *et al*. observed a decrease in luminescence intensity and increase in the 108-cm^{-1} Raman band of $CH_3NH_3PbI_3$ solar cells and attributed these changes to slow photoinduced structural changes since the timescale of the change was not consistent with an electronic process.[31] Sadhanala and co-workers measured two absorption peaks in freshly-prepared, mixed-halide ($CH_3NH_3Pb(Br_{1-x}I_x)_3$ perovskite films. A single absorption band, however, was measured after aging the film for 21 days.[30] Hoke *et al*. have also reported light-induced changes to the absorption and photoluminescence spectra of $CH_3NH_3Pb(Br_{1-x}I_x)_3$ perovskite films. They attribute these behaviors to reversible crystalline changes and trap states [29]. Structural defects may also account for the notorious photocurrent hysteresis[32,33] and increased quantum efficiency with heavier halide species[34] that characterizes perovskite semiconductors and devices. Unusual photo physics that are caused by surface defects may become even more prominent in nanocrystalline perovskites.[35]

Trap states in perovskites. $CH_3NH_3PbI_3$ has a broad emission band and a high quantum yield of photoluminescence. The nature of the radiative decay channels and the spectral broadening mechanisms are largely determined by phonon coupling effects and defects or trap states [36]. Trap states are more problematic near surfaces and interfaces since they are the locations where defects to the perovskite crystal structure are most likely to occur.[35] Vacancies, such as ionic defects like Pb^+, I^-, and $CH_3NH_3^+$, can also form shallow trap states and reduce carrier lifetimes.[37] Strong covalency of the Pb cations and I anions lead to the formation of Pb dimers and iodide trimers, which are responsible for transition levels that can serve as recombination centers that reduce solar-cell performance.[38] Trap states increase the frequency of non-radiative recombination, which reduces the QY [39]. Density-functional theory studies have

revealed the unusual defect physics of $CH_3NH_3PbX_3$ [37,38,40-42]. For example, shallow point defects partially explain ultra-high open-circuit voltages of $CH_3NH_3PbBr_3$ solar cells.[42]

Synthetic conditions play an important role in the formation of trap states. For example, perovskites grown under high iodine concentrations are likely to have defects (lead atom substituted by iodide) and a high density of deep electronic traps (recombination centers) that cause short diffusion lengths and poor photovoltaic performance [43]. Supramolecular halogen bond complexation can passivate the under-coordinated iodine ions, which can reduce trap sites near the perovskite surface;[44] whereas Lewis bases are used to passivate under-coordinated lead atoms, and treated perovskites exhibited reduced electron-hole recombination and a consequently longer photoluminescence lifetimes.[45] Adding fullerene layers has also proven to be an effective way to passivate the charge trap states and get rid of photocurrent hysteresis.[32,46]

Building on our previous work,[24] a systematic synthesis of photostable nanocrystalline $CH_3NH_3PbX_3$ is demonstrated. Optimization of the $CH_3NH_3PbI_3$ alkyl halide to lead halide precursor ratio inhibited the appearance of a reversible photoinduced 630-nm photoluminescence peak that may be derived from surface traps. Using an optimized synthetic procedure, luminescence of single $CH_3NH_3PbI_3$ and $CH_3NH_3PbBr_3$ nanocrystals was stable over 240 seconds with over 1×10^5 W/cm^2 irradiance. The reported optimized synthesis may be applicable to other organometal halide perovskites, for example those with mixed halide composition.

2.2. Experimental

2.2.1 Materials

Lead (II) bromide ($\geq$ 98%), N, N-dimethylformamide (DMF), Lead (II) iodide (99%), methylamine (33 wt% in ethan ol), *n*-octylamine (99%), and (anhydrous, 99.8%) were purchased from Sigma-Aldrich. Hydrobromic acid (ACS, 47.0-49.0%), hydroiodic acid (ACS, 55-58%),

and oleic acid (tech., 90%) from Alfa-Aesar; diethyl ether from Baker; toluene (99.9%) and acetonitrile (99.9%) from Fisher. Materials were used as received unless specified otherwise.

2.2.2 Synthesis

Ammonium Halides. Dimensionality control is achieved using a bulky alkylammonium cation as a capping ligand. Hydrogen halides were prepared by a modified literature procedure.[37] Briefly, hydroiodic acid (10 mL, 0.075 mol) or hydrobromic acid (8.6 mL, 0.075 mol) was added to a solution of excess methylamine (24 mL, 0.192 mol) in ethanol (100 mL) at 0 °C, and the mixture stirred at this temperature for 2 h. The sample was concentrated under vacuum, and the resulting powder dried under dynamic vacuum at 60 °C for 12 h and recrystallized from ethanol. Both *n*-octyl ammonium iodide ($CH_3(CH_2)_7NH_3I$) and *n*-octyl ammonium bromide ($CH_3(CH_2)_7NH_3Br$) were washed repeatedly with diethyl ether and dried under dynamic vacuum before use.

Nanocrystalline $CH_3NH_3PbX_3$. PbX_2 (0.008 mmol), CH_3NH_3X (0.012 mmol) and $CH_3(CH_2)_7NH_3X$ (0.012 mmol) were dissolved in a mixture of acetonitrile (20 mL) and DMF (200 µL). 4 mL of the resulting precursor solution was rapidly injection into toluene (15 mL) while stirring. After 24 h stirring at 20 °C, solids were isolated by centrifugation (10 min at 4000 rpm) and purified by washing with toluene (5 mL) followed by re-centrifugation.

2.2.3 Structural Characterization

X-Ray Diffraction (XRD) was collected on a Rigaku Ultima IV (40 kV, 44 mA). A Cu KR source was used for radiation. A quartz sample holder was used as a substrate for drop-casted toluene solvated samples. Details of the *in situ* measurements were as previously reported.[47] Transmission Electron Microscopy (TEM) images were collected using a FEI Technai G2 F20 field-emission TEM capable of 200 kV with a point-to-point resolution of less than 0.25 nm

having a 0.10-nm line-to-line resolution. Dilute solutions were prepared in toluene and 2 to 3 drops of each product were placed onto carbon-coated copper grids. TEM was used to measure the particle dimensions and processed using the ImageJ program. Typically more than 100 particles were counted in each case. Uncertainties in all measurements are reported as standard deviations.

2.2.4 Optical Characterization

Solution-phase optical extinction (absorption plus scattering) spectra were collected using an Agilent 8453 UV/Vis spectrophotometer equipped with a photodiode array. Solvent absorption was subtracted from all spectra. Drop-casted solid films of each sample was measured using diffuse reflectance (SL1 Tungsten Halogen lamp (vis-IR), a SL3 Deuterium Lamp (UV), and a BLACK-Comet C-SR-100 Spectrometer). A Horiba-Jobin Yvon Nanolog scanning spectrofluorometer equipped with a photomultiplier detector was used to collect steady-state PL spectra. Quantum yields for each nanocrystalline perovskite were determined comparing luminescence intensities of phodamine 590 or 640.[48]

For the luminescence micro spectroscopy of single nanocrystals, a DM IRBE microscope (Leica, Wetzlar, Germany) was employed. Monochromatic illumination at 532 nm (Coherent, Santa Clara, CA) was used to excite $CH_3NH_3PbI_3$; and, at 488 nm (Argon Ion 488 nm, Uniphase, San Jose, CA) for $CH_3NH_3PbBr_3$. An oil-immersion (Leica, 100× HCX PL APO, 1.49 numerical aperture) having a sample area diameter of 0.28 ± 0.03 μm was used providing an excitation power density of 1.6×10^5 W·cm^{-2}. PL was collected using a HoloSpec f/1.8i spectrograph (Kaiser Optical Systems, Ann Arbor, MI, USA), equipped with a broad-range grating (HFG-650, Kaiser Optical Systems) and a charged-coupled device (CCD) (Newton 940,

Andor Technology, Belfast, UK) with a collection binning time of 0.05 s. 2400 spectra were collected every 0.09873 seconds.

2.3. Results and Discussion

2.3.1 General Synthesis and Characterization

Nanocrystalline organ lead halide perovskites are prepared by dissolving PbX_2 (a), CH_3NH_3X (b), and $CH_3(CH_2)_7NH_3X$ (c) precursors (X = I or Br) in a polar solvent such as dimethyl formamide (DMF, $\varepsilon = 38.25$) or acetonitrile ($\varepsilon = 36.64$), followed by quick injection into a less polar solvent such as toluene ($\varepsilon = 2.379$) as shown in Scheme 1.[22] DMF, acetonitrile, or both are used because they provide excellent precursor solubility, as we reported previously for the synthesis of perovskite nanowires.[22] Introduction of a large ionic ligand, such as an ammonium or carboxylate-containing surfactant, decreases the perovskite particle size. In this study, the concentration of the CH_3NH_3X and larger alkyl ammonium halide, n-$CH_3(CH_2)_7NH_3X$, are equivalent. In this way low-dimensional (nanocrystalline) perovskites are synthesized.[16,35,49] Perovskite nanocrystals produced by this method contain methyl ammonium cations within their core, and octyl ammonium groups on their surface.[50]

$$PbX_2 + 3\ CH_3NH_3X + 3\ C_8H_{17}NH_3X \xrightarrow[\text{(2) Toluene}]{\text{(1) CH}_3\text{CN and/or DMF}} (CH_3NH_3)_{1-z}(C_8H_{17}NH_3)_z PbX_3$$
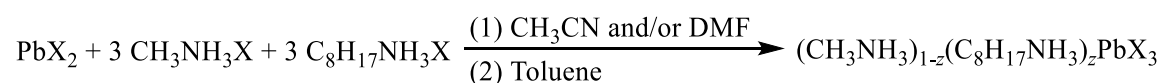
Scheme 2.1. Synthesis of nanocrystalline organ lead halide (X = Br or I) perovskites prepared using a molar concentration of alkylammonium halide precursor that is 3× higher than that of the lead halide precursor; $0 < z \ll 1$.

During the synthesis of iodide perovskites, the PbI_2 precursor fails to dissolve completely in the co-solvent unless an excess of ammonium halide precursors is present. A very large excess of ammonium halides, however, irreversibly affects the optical properties of the resulting perovskites, as discussed below. Precursor reactivities and ease of forming solid solutions also

affect the product. CH_3NH_3X salts dissociate differently in DMF depending on the specific halide (Scheme 2). For iodide, the preferred products are $CH_3NH_3^+$ and I^-, the conjugate base of HI, which is a strong acid in DMF and leads to a large conductivity (Scheme 2, Figure 1 when $[PbX_2]_T = 0$). For bromide the preferred products are CH_3NH_2 along with HBr, which is a weaker acid in DMF and leads to a smaller conductivity (Scheme 2, Figure 1 when $[PbX_2]_T = 0$). Thus, CH_3NH_3I is expected to be the most reactive ammonium halide precursor in DMF, generating free and readily available I^- needed for perovskite formation that should be easily precipitated upon addition of a nonpolar solvent such as toluene.

$$CH_3NH_3X \underset{(b)}{\overset{(a)}{\longleftarrow}} \begin{array}{c} DMF \\ \end{array} \begin{array}{c} \nearrow CH_3NH_3^+ + X^- \\ \Updownarrow \\ \searrow CH_3NH_2 + HX \end{array}$$
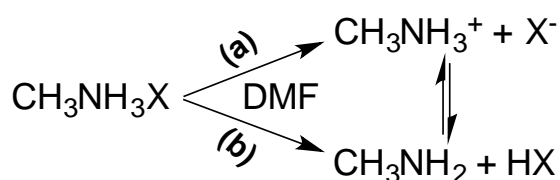
Scheme 2.2. Pathways of CH3NH₃X dissociation in DMF.

To probe PbX_2 precursor reactivity, we measured their specific conductivities (κ) in DMF with both the presence and absence of a set amount of the corresponding CH_3NH_3X (Fig. 2.1). As expected, in pure DMF, the conductivity increases linearly with PbX_2 concentration. Conductivity is proportional to the number of ions in solution, thus enabling a comparison to the relative degree of dissociation and association. A steeper increase for the iodide case suggests that dissociation is slightly higher for PbI_2 than for $PbBr_2$. With the presence of 50 mM CH_3NH_3X in DMF, the conductivity actually decreases upon addition of PbI_2 and slowly increases upon addition of $PbBr_2$. When a 1 to 3 ratio of PbX_2 to CH_3NH_3X is used, as is the case in the Scheme 1 perovskites, the conductivity is higher for PbI_2/CH_3NH_3I than $PbBr_2/CH_3NH_3Br$

suggesting that Pb-Br binding in solution is stronger than Pb-I binding. A similar observation

was reported by luminescence and transient absorption measurements.[51]
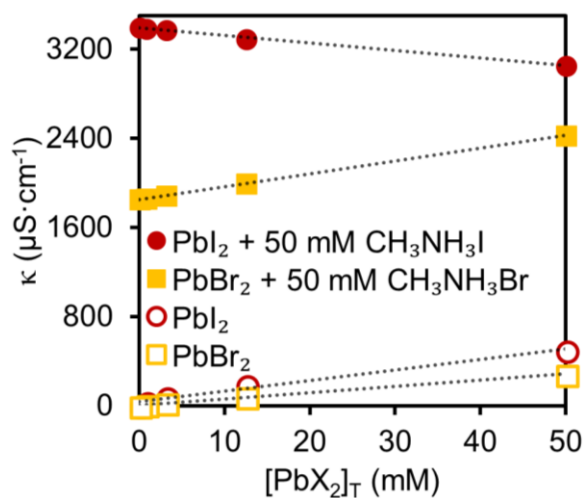
Figure 2.1. Specific conductivity (κ) *vs.* PbX_2 concentration with (solid) or without (hollow) 50 mM CH_3NH_3X.

Structural Analysis. Powder X-ray diffraction (XRD) patterns show the diffraction peaks

corresponding to the <110> and <001> facets of the $CH_3NH_3PbI_3$ and $CH_3NH_3PbBr_3$

nanocrystals (Fig. 2.2). The bromide perovskites shift to higher 2 theta values since bromine has

a higher electronegativity compared to iodine, indicating some degree of solid solution,

consistent with literature.[52,53] Table 2.1 presents the lattice parameter of cubic (or pseudo-cubic,

in the case of $CH_3NH_3Pb_3$) determined experimentally from the powder XRD data for both the

$CH_3NH_3PbBr_3$ and $CH_3NH_3PbI_3$ nanocrystalline perovskites. The lattice parameter is equal in all

directions for the $CH_3NH_3PbBr_3$ material, while it is distorted in one dimension for the

$CH_3NH_3PbI_3$ counterpart.
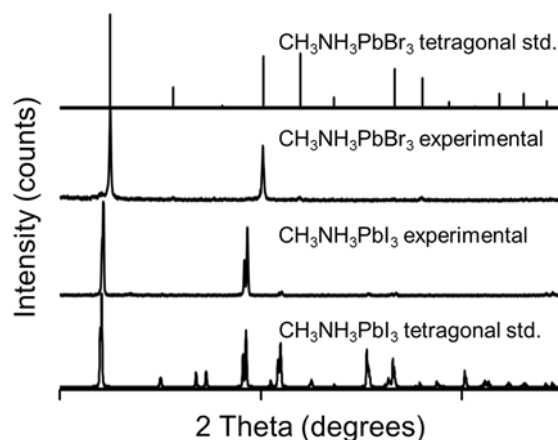
Fig. 2.2. Powder XRD of nanocrystalline organometal halide perovskites with corresponding standard (std.) diffraction patterns. The red and green dashed lines correspond to the strongest (110) and (001) diffraction peaks in the standard patterns of iodide and bromide perovskites.

The transmission electron microscopy (TEM) images shown in Fig. 2.3 reveal that the perovskites are primarily made of nanospheres with an average size of 7 ± 2 nm for $CH_3NH_3PbI_3$ and 8 ± 2 nm $CH_3NH_3PbBr_3$. The Bohr radii for bromide and iodide perovskites are 2 and 2.2 nm, respectively.[54] In addition to the nanospheres, the $CH_3NH_3PbBr_3$ perovskites exhibit nanosheets making up *ca.* 10-20% of the total particles. As we previously reported, perovskite nanosheets are unstable under the TEM electron beam [22]. The presence of nanosheets is a contributing factor for the preferred orientation behavior observed by powder XRD for $CH_3NH_3PbI_3$ perovskite nanocrystals.
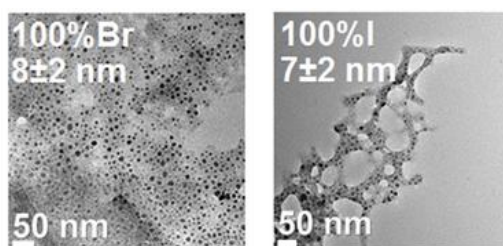
Fig. 2.3. Representative TEM images of $CH_3NH_3PbBr_3$ and $CH_3NH_3PbI_3$ nanocrystalline perovskites.

3.2 Optical Properties and Photostability

Using a spectrofluorometer with arc lamp illumination and solution-based measurements, the

λ_{max} for $CH_3NH_3PbI_3$ is 760 nm; and for $CH_3NH_3PbBr_3$, 518 nm. This is consistent with

literature reports for perovskites of similar composition.[55-57] The $CH_3NH_3PbBr_3$ perovskite

sample has a 29-fold higher photoluminescence quantum yield (44%) compared to $CH_3NH_3PbI_3$

(Table 2.1).

Table 2.1. Characterization parameters of low-dimensional organometal halide perovskites.
[1] lattice parameter (a)
[2] More than 100 nanocrystals measured

Loading	a (nm)[1]	Scherrer Size (nm)	TEM[2] Size (nm)	Abs. Edge (nm)	First-Exciton Luminescence (nm)	Quantum Yield (%)
$CH_3NH_3PbBr_3$	0.587	7	8±2	527	506	44
$CH_3NH_3PbI_3$	0.634	>100	7±2	774	745	1.5

Nanocrystalline perovskites prepared using Scheme 1 with an a: b:c precursor ratio of

1:3:3 exhibited two luminescence peaks in a flash photolysis experiment with nanosecond pulsed

NdYAG laser illumination. One peak had a λ_{max} at 745 nm (E_g) and the second peak had a λ_{max}

at 642 nm ($E>E_g$) for $CH_3NH_3PbI_3$ and 0.01 mJ pulsed-laser illumination (Fig 4a). With

increasing excitation energy the relative intensity of the 642 nm peak increases nonlinearly (Fig

4b) and both peaks blue shift. With 12-mJ illumination, the λ_{max} are 626 nm and 725 nm.
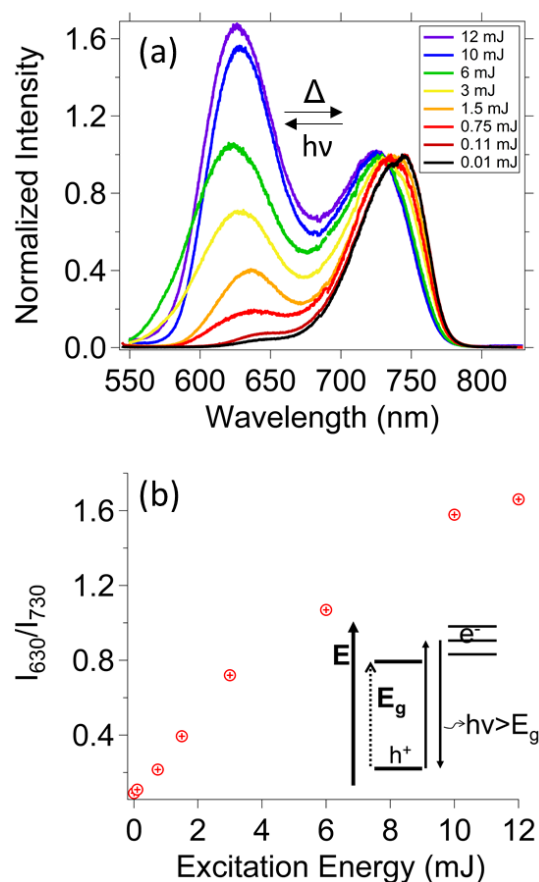
Fig. 2.4. (a) Flash photolysis luminescence spectra of nanocrystalline $CH_3NH_3PbI_3$, prepared using Scheme 1, as a function of excitation power. The spectra are normalized to the intensity at ~745 nm (at the λ_{max}). (b) Intensity ratios of the ~642nm (I_{642}) and ~745 nm (I_{745}) bands vs. incident laser power. The insert explains the band gap (E_g) of the nanocrystalline perovskite vs the higher energy trap state luminescence.

To determine if the photoinitiated increase in the 642 nm peak intensity was reversible, the luminescence spectrum of the $CH_3NH_3PbI_3$ nanocrystals was monitored in a new-batch of nanocrystals after blocking the laser irradiation. After 300 minutes in the dark, the intensity of the band at 642 nm decreased due to a thermal relaxation mechanism. The photoinitiated reversible spectral changes may be the result of changes in the crystal phase or the population of surface traps.
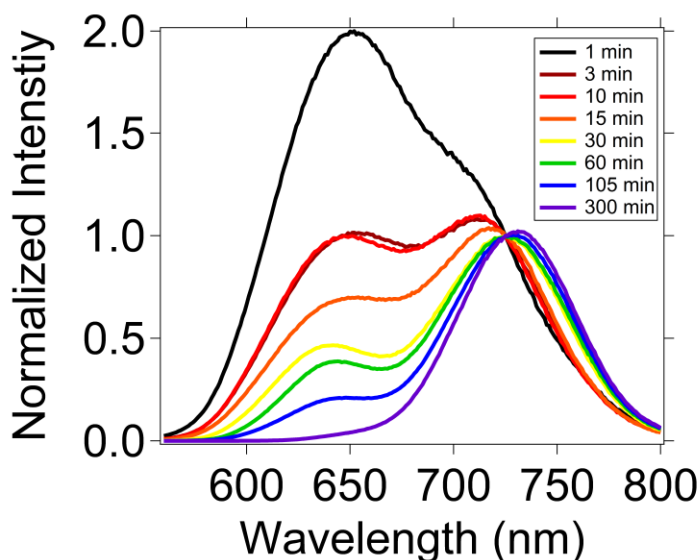
Fig. 2.5. Flash photolysis luminescence spectra of nanocrystalline $CH_3NH_3PbI_3$ made with Scheme 1 showing thermal relaxation subsequent to laser illumination from a 532-nm, 15-mJ Nd:YAG providing nanosecond pulses. Time zero corresponds to the time when the laser was blocked from illuminating the sample.

In order to rule out phase changes as the cause of the photoinduced spectral changes, we conducted *in situ* XRD experiments[47] to search for possible structural changes in the nanocrystalline perovskites during illumination with a pulsed laser. An open window was used to the laser to irradiate the samples while mounted in the XRD instrument. The nanocrystalline material was in the solid state so no solvent effects were present. The $CH_3NH_3PbI_3$ nanocrystalline perovskites exhibited no change in 2θ diffraction peak location or new peaks as a result of irradiation with a laser energy up to 15 mJ (Fig. 2.6). The *in situ* XRD analysis revealed no additional or shifted diffraction peaks, which indicates that a phase transition does not occur upon illumination.
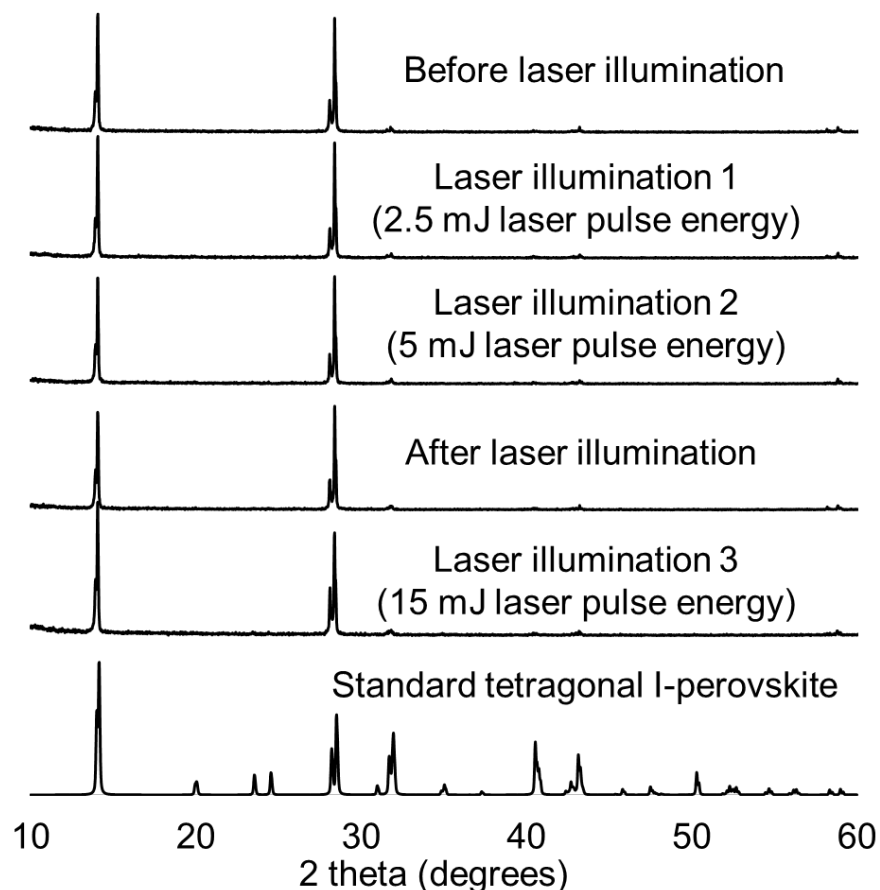
Fig. 2.6. X-ray diffraction patterns from nanocrystalline CH₃NH₃PbI₃ perovskites at different pulse energies. The laser illuminated the sample during the entire time XRD data were collected.

Since a phase change was not measured upon irradiating the sample, the photoinitiated blue photoluminescence peak may result from surface trap states that are populated upon irradiation. In this case, the perovskites have traps with energies above the conduction band that emit at higher energies than the band gap (Fig 4b inset). An increasing population in trap states with increasing irradiation power could explain the increasing intensity of the 630-nm peak in going from 0.01 mJ to 12 mJ (Fig. 2.4). Excess precursor may lead to higher energy emissive states which differ from the traditional nanocrystalline lattice expected for CH₃NH₃PbI₃ nanocrystals. By using a precursor ratio of 1:1.5:1.5 (Scheme 2), the CH₃NH₃PbBr₃ and

$CH_3NH_3PbI_3$ exhibited only one luminescence peak at 540 nm and 800 nm, respectively (Fig. 2.7a, 2.8a). The disappearance of a second luminescence peak illustrates that bromide and iodide nanocrystalline perovskites prepared using Scheme 2 each have a single emitting state compared to the multiple emitting states observed for the nanocrystals prepared using Scheme 1 with a higher precursor ratio. This observation supports the hypothesis that a synthesis using the smaller ratio of precursors may result in nanocrystals with higher crystalline order and fewer defects compared to a synthesis using a larger precursor ratio.

$$PbX_2 + 1.5\ CH_3NH_3X + 1.5\ C_8H_{17}NH_3X \xrightarrow[\text{(2) Toluene}]{\text{(1) } CH_3CN \text{ and/or DMF}} (CH_3NH_3)_{1-z}(C_8H_{17}NH_3)_zPbX_3$$
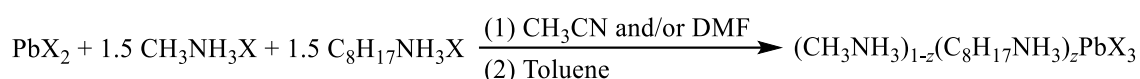
Scheme 2.3. Optimized synthesis of nanocrystalline organ lead halide (X = I or Br) perovskites prepared using a molar concentration of alkylammonium halide precursor that is 1.5× that of the lead halide precursor; $0 < z << 1$.

To examine the stability and of perovskites prepared using the optimized synthetic method with prolonged illumination, fluorescence micro spectroscopy of individual nanocrystals was employed. For this experiment, a batch of 24-hour-aged perovskites in toluene was divided into four samples. One sample was left as is, and is referred to as the "unwashed sample." The second sample was mixed with additional 0.012-mM alkylammonium halide (*i.e.*, the same concentration as the precursor solution) and was labeled "unwashed with excess precursor." For the third and fourth samples, the perovskites were precipitated from the product solution and were resuspended in toluene ("washed sample") or a 0.01- mM alkylammonium halide solution in toluene ("washed with excess precursor sample").
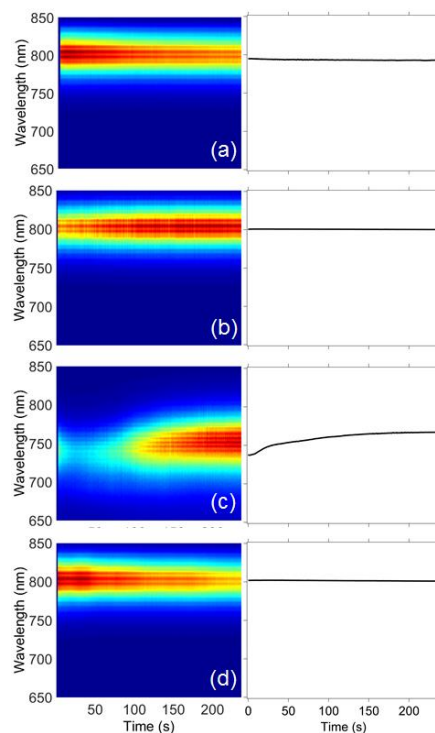
Fig. 2.7 Time-correlated luminescence micro spectroscopy spectra of single $CH_3NH_3PbI_3$ perovskites. The left column shows the plots show luminescence versus illumination time with a 532 nm laser (1.58×10^5 W/cm^2) for $CH_3NH_3PbI_3$ perovskites synthesized using Scheme 2. The samples are: (a) unwashed sample, (b) washed sample, (c) unwashed with excess precursor, and (d) washed with excess precursor sample. The right column shows the average λ_{max} versus illumination time (n=3).

The $CH_3NH_3PbI_3$ perovskites prepared using Scheme 2 exhibited a constant λ_{max} of 800 nm for all samples except the unwashed sample that had added precursor. For the latter, the λ_{max} shifts from 737 nm at the start of illumination to 767 nm after 240 s of illumination. Thus, for $CH_3NH_3PbI_3$ additional precursor affects the photostability whether it is present during the synthesis or added post synthesis. While the λ_{max} is stable for most of the $CH_3NH_3PbI_3$ samples, the luminescence intensity is variable over the measurement period and photo brightening or photobleaching was measured for most of the nanocrystals (Fig. S2.2). We have previously reported and discussed this behavior [57]. The nanocrystalline $CH_3NH_3PbBr_3$ perovskites prepared using the optimized synthesis (Scheme 2) exhibited a constant luminescence λ_{max} around 540 nm

(Fig. 2.8) for all samples, even when additional precursor was added to the washed nanocrystals. (No shifts of λ_{max} greater than 4nm were measured). This indicates that the higher precursor concentration must be present during the synthesis to have an effect on generating the photoinitiated luminescence peaks for $CH_3NH_3PbBr_3$. Photo brightening and photobleaching were also recorded for $CH_3NH_3PbBr_3$ nanocrystals (Fig. S2.3). Freppon et al report the emission of these nanocrystals to be 498 nm. This reported wavelength was measured in toluene.[57] The red shift in λ_{max} can be accounted for the time-correlated luminescence spectra being collected in a dry state.
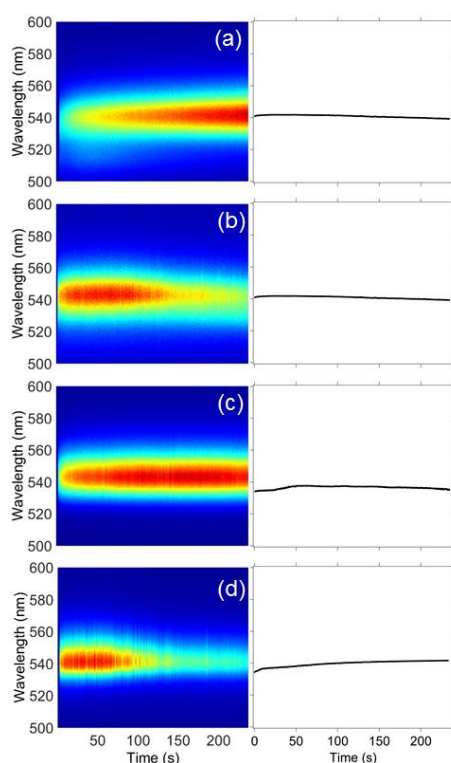
Fig. 2.8 Time-correlated luminescence micro spectroscopy spectra of single $CH_3NH_3PbBr_3$ perovskites. The left column shows the plots show luminescence versus illumination time with a 488 nm laser (1.58×10^5 W/cm^2) for $CH_3NH_3PbBr_3$ perovskites synthesized using Scheme 2. The samples are: (a) unwashed sample, (b) washed sample, (c) unwashed with excess precursor, and (d) washed with excess precursor sample. The right column shows the average λ_{max} versus illumination time (n=3). Any deviations in λ_{max} are less than 4 nm, and can be explained as measurement uncertainty (e.g., minor changes to the focus).

Hu et al. measured no shifts in the emission λ_{max} for $CsPbI_3$ nanocrystals for more than 240 seconds when excited using a pulsed laser with an average power between 2 and 10 nW.[58] They only reported spectra for two nanocrystals, so it is not possible to determine if this behavior is representative of all nanocrystals in their sample. Nine of the $CH_3NH_3PbI_3$ nanocrystals we measured exhibited similar stable luminescence behavior while three showed a shift in λ_{max} as much as 79 nm. Eight of the $CH_3NH_3PbBr_3$ nanocrystals we measured exhibited stable luminescence behavior while four showed a shift in λ_{max} as much as 8 nm. Rainò et al. also observed a shift in the emission λ_{max} in mixed halide $CsPb(Br/Cl)_3$ nanocrystals from (224 to 224.2 nm).[59]

4. Conclusion

In order to be useful in a variety of applications, nanocrystalline perovskites need to be photostable. The non-optimized organometal halide perovskites show shifts in luminescence λ_{max} and exhibit multiple luminescence peaks when excess alkylammonium precursor is used. The optimized synthetic method produces nanocrystalline methylammonium lead halide particles that are photostable over at least 4 minutes of focused illumination. The mechanism for the improved photostability is likely to be reduced surface traps when low precursor ratios are utilized. Similar synthetic methods may increase the photostability of related perovskites. This work reports on the photostability of perovskites containing a single halide. In the case of mixed-halide perovskite nanocrystals, where domains of heterogeneous halide compositions may exist, the photostability is more complicated. For example, our initial investigation has shown that $CH_3NH_3Pb(Br_{0.2}I_{0.8})_3$ nanocrystalline perovskites exhibit an abrupt shift in λ_{max} from 630 nm to 750 nm after a few seconds of illumination followed by a constant λ_{max} with additional illumination (Fig S4). Under the same experimental and measurements conditions, single-halide

perovskites exhibit stable λ_{max} as reported in this work. Thus, the continued study of mixed-halide perovskites should be pursued.

Acknowledgements

Chapter 2 Supplemental Information
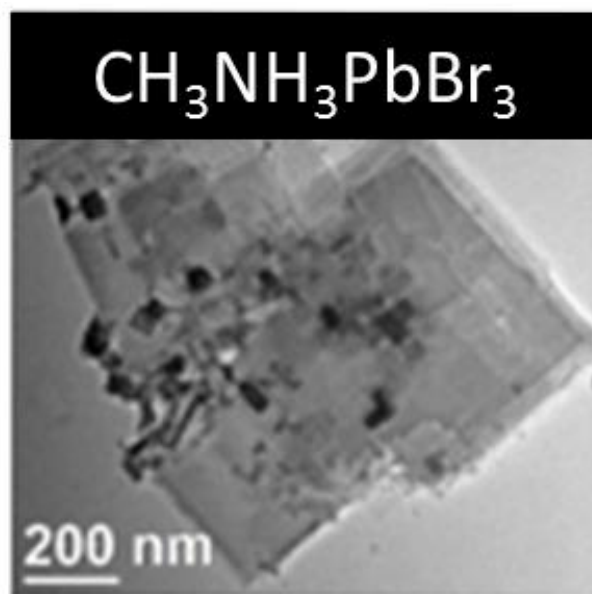
Figure S2.1. TEM image of nanocrystalline $CH_3NH_3PbBr_3$ perovskites showing sheet morphology. L = 164 ± 170 nm.
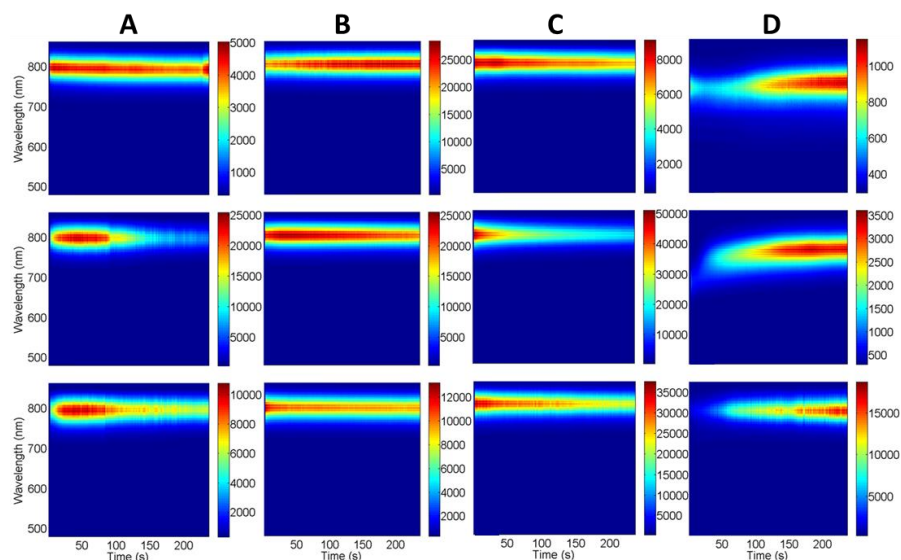
Figure S2.2. Time-correlated luminescence micro spectroscopy spectra of single CH$_3$NH$_3$PbI$_3$ perovskites. The plots show luminescence versus illumination time of 3 individual nanocrystals with a 532-nm laser (1.58 × 10^5 W/cm^2) for CH$_3$NH$_3$PbI$_3$ perovskites synthesized using Scheme 2. The samples are: (column A) unwashed sample, (column B) washed sample, (column C) unwashed with excess precursor, and (Column D) washed with excess precursor sample.
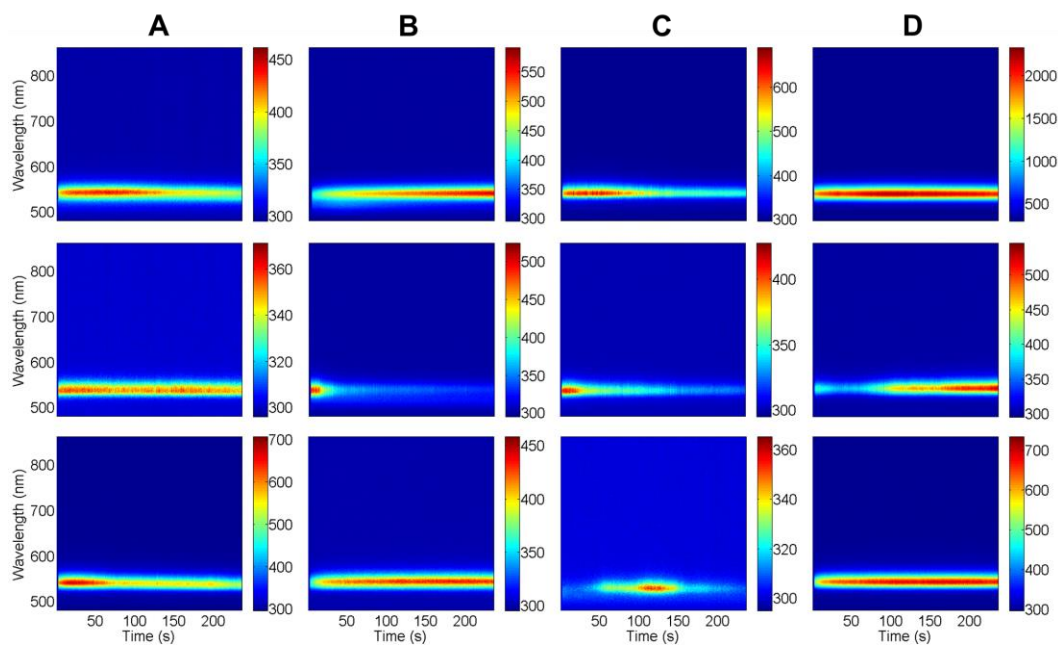
Figure S2.3. Time-correlated luminescence micro spectroscopy spectra of single CH$_3$NH$_3$PbBr$_3$ perovskites. The plots show luminescence versus illumination time of 3 individual nanocrystals with a 532-nm laser (1.58 × 10^5 W/cm^2) for CH$_3$NH$_3$PbBr$_3$ perovskites synthesized using Scheme 2. The samples are: (column A) unwashed sample, (column B) washed sample, (column C) unwashed with excess precursor, and (Column D) washed with excess precursor sample.
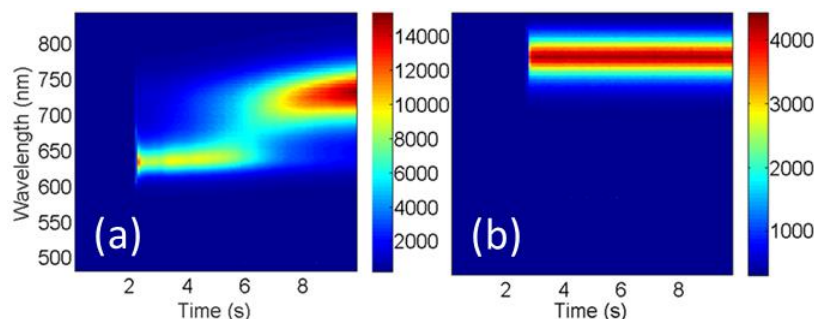
Figure S2.4. Time-correlated luminescence micro spectroscopy spectra of single (a) CH₃NH₃Pb(I₀.₈Br₀.₂)₃ and (b) CH₃NH₃PbI₃ perovskite nanocrystals versus time. The 532-nm continuous-wave laser illumination was blocked for the first 2 seconds of data collection to ensure that fast photophysical events were captured in the data recording.

References

(1)   Green, M. A.; Ho-Baillie, A. *ACS Energy Letters* **2017**, *2*, 822.

(2)   Li, Z.; Klein, T. R.; Kim, D. H.; Yang, M.; Berry, J. J.; van Hest, M. F.; Zhu, K. *Nature Reviews Materials* **2018**, *3*, 18017.

(3)   Sutherland, B. R.; Sargent, E. H. *Nature Photonics* **2016**, *10*, 295.

(4)   Dong, Q.; Fang, Y.; Shao, Y.; Mulligan, P.; Qiu, J.; Cao, L.; Huang, J. *Science* **2015**, *347*, 967.

(5)   Kojima, A.; Teshima, K.; Shirai, Y.; Miyasaka, T. *Journal of the American Chemical Society* **2009**, *131*, 6050.

(6)   Liu, M.; Johnston, M. B.; Snaith, H. J. *Nature* **2013**, *501*, 395.

(7)   Burschka, J.; Pellet, N.; Moon, S.-J.; Humphry-Baker, R.; Gao, P.; Nazeeruddin, M. K.; Grätzel, M. *Nature* **2013**, *499*, 316.

(8)   Zhou, H.; Chen, Q.; Li, G.; Luo, S.; Song, T.-b.; Duan, H.-S.; Hong, Z.; You, J.; Liu, Y.; Yang, Y. *Science* **2014**, *345*, 542.

(9)   Yang, W. S.; Noh, J. H.; Jeon, N. J.; Kim, Y. C.; Ryu, S.; Seo, J.; Seok, S. I. *Science* **2015**, *348*, 1234.

(10)   Yang, W. S.; Park, B.-W.; Jung, E. H.; Jeon, N. J.; Kim, Y. C.; Lee, D. U.; Shin, S. S.; Seo, J.; Kim, E. K.; Noh, J. H. *Science* **2017**, *356*, 1376.

(11)   Christians, J. A.; Miranda Herrera, P. A.; Kamat, P. V. *Journal of the American Chemical Society* **2015**, *137*, 1530.

(12)   Bert, C.; Jeroen, D.; Nicolas, G.; Aslihan, B.; Jan, D. H.; Lien, D. O.; Anitha, E.; Jo, V.; Jean, M.; Edoardo, M.; De, A. F.; Hans-Gerd, B. *Advanced Energy Materials* **2015**, *5*, 1500477.

(13)   Berhe, T. A.; Su, W.-N.; Chen, C.-H.; Pan, C.-J.; Cheng, J.-H.; Chen, H.-M.; Tsai, M.-C.; Chen, L.-Y.; Dubale, A. A.; Hwang, B.-J. *Energy & Environmental Science* **2016**, *9*, 323.

(14)   Samrana, K.; Khaja, N. M.; Michael, G.; Shahzada, A. *Angewandte Chemie International Edition* **2014**, *53*, 2812.

(15)   Gao, P.; Grätzel, M.; Nazeeruddin, M. K. *Energy & Environmental Science* **2014**, *7*, 2448.

(16)   Dou, L.; Wong, A. B.; Yu, Y.; Lai, M.; Kornienko, N.; Eaton, S. W.; Fu, A.; Bischak, C. G.; Ma, J.; Ding, T. *Science* **2015**, *349*, 1518.

(17)   Boix, P. P.; Agarwala, S.; Koh, T. M.; Mathews, N.; Mhaisalkar, S. G. *The Journal of Physical Chemistry Letters* **2015**, *6*, 898.

(18)   Sichert, J. A.; Tong, Y.; Mutz, N.; Vollmer, M.; Fischer, S.; Milowska, K. Z.; García Cortadella, R.; Nickel, B.; Cardenas-Daw, C.; Stolarczyk, J. K. *Nano Letters* **2015**, *15*, 6521.

(19)   Protesescu, L.; Yakunin, S.; Bodnarchuk, M. I.; Krieg, F.; Caputo, R.; Hendon, C. H.; Yang, R. X.; Walsh, A.; Kovalenko, M. V. *Nano Letters* **2015**, *15*, 3692.

(20)   Deschler, F.; Price, M.; Pathak, S.; Klintberg, L. E.; Jarausch, D.-D.; Higler, R.; Hüttner, S.; Leijtens, T.; Stranks, S. D.; Snaith, H. J.; Atatüre, M.; Phillips, R. T.; Friend, R. H. *The Journal of Physical Chemistry Letters* **2014**, *5*, 1421.

(21)   Zhang, F.; Zhong, H.; Chen, C.; Wu, X.-g.; Hu, X.; Huang, H.; Han, J.; Zou, B.; Dong, Y. *ACS Nano* **2015**, *9*, 4533.

(22)   Zhu, F.; Men, L.; Guo, Y.; Zhu, Q.; Bhattacharjee, U.; Goodwin, P. M.; Petrich, J. W.; Smith, E. A.; Vela, J. *ACS Nano* **2015**, *9*, 2948.

(23)   Tan, Z.-K.; Moghaddam, R. S.; Lai, M. L.; Docampo, P.; Higler, R.; Deschler, F.; Price, M.; Sadhanala, A.; Pazos, L. M.; Credgington, D.; Hanusch, F.; Bein, T.; Snaith, H. J.; Friend, R. H. *Nature Nanotechnology* **2014**, *9*, 687.

(24)   Zhang, M.; Yu, H.; Lyu, M.; Wang, Q.; Yun, J.-H.; Wang, L. *Chemical Communications* **2014**, *50*, 11727.

(25)   Jang, D. M.; Park, K.; Kim, D. H.; Park, J.; Shojaei, F.; Kang, H. S.; Ahn, J.-P.; Lee, J. W.; Song, J. K. *Nano Letters* **2015**, *15*, 5191.

(26)   Noh, J. H.; Im, S. H.; Heo, J. H.; Mandal, T. N.; Seok, S. I. *Nano Letters* **2013**, *13*, 1764.

(27)   Dimesso, L.; Dimamay, M.; Hamburger, M.; Jaegermann, W. *Chemistry of Materials* **2014**, *26*, 6762.

(28)   Misra, R. K.; Aharon, S.; Li, B.; Mogilyansky, D.; Visoly-Fisher, I.; Etgar, L.; Katz, E. A. *The Journal of Physical Chemistry Letters* **2014**, 326.

(29)   Hoke, E. T.; Slotcavage, D. J.; Dohner, E. R.; Bowring, A. R.; Karunadasa, H. I.; McGehee, M. D. *Chemical Science* **2015**, *6*, 613.

(30)   Sadhanala, A.; Deschler, F.; Thomas, T. H.; Dutton, S. E.; Goedel, K. C.; Hanusch, F. C.; Lai, M. L.; Steiner, U.; Bein, T.; Docampo, P.; Cahen, D.; Friend, R. H. *The Journal of Physical Chemistry Letters* **2014**, *5*, 2501.

(31)   Gottesman, R.; Gouda, L.; Kalanoor, B. S.; Haltzi, E.; Tirosh, S.; Rosh-Hodesh, E.; Tischler, Y.; Zaban, A.; Quarti, C.; Mosconi, E. *The Journal of Physical Chemistry Letters* **2015**, *6*, 2332.

(32)   Shao, Y.; Xiao, Z.; Bi, C.; Yuan, Y.; Huang, J. *Nature communications* **2014**, *5*, 5784.

(33)   Yuan, Y.; Huang, J. *Accounts of chemical research* **2016**, *49*, 286.

(34)   Stranks, S. D.; Burlakov, V. M.; Leijtens, T.; Ball, J. M.; Goriely, A.; Snaith, H. J. *Physical Review Applied* **2014**, *2*, 034007.

(35)   Wu, X.; Trinh, M. T.; Niesner, D.; Zhu, H.; Norman, Z.; Owen, J. S.; Yaffe, O.; Kudisch, B. J.; Zhu, X.-Y. *Journal of the American Chemical Society* **2015**, *137*, 2089.

(36)   Wehrenfennig, C.; Liu, M.; Snaith, H. J.; Johnston, M. B.; Herz, L. M. *The Journal of Physical Chemistry Letters* **2014**, *5*, 1300.

(37)   Kim, J.; Lee, S.-H.; Lee, J. H.; Hong, K.-H. *The Journal of Physical Chemistry Letters* **2014**, *5*, 1312.

(38)   Agiorgousis, M. L.; Sun, Y.-Y.; Zeng, H.; Zhang, S. *Journal of the American Chemical Society* **2014**, *136*, 14570.

(39)   Sangni, W.; Furong, H.; Liya, Z.; Jianwu, W.; Youling, X.; Peng, J.; Zhuo, C.; Zuodong, Y.; Qi, P.; Zhong, Z. J. *ChemNanoMat* **2018**, *4*, 409.

(40)   Yin, W.-J.; Shi, T.; Yan, Y. *Applied Physics Letters* **2014**, *104*, 063903.

(41)   Wan-Jian, Y.; Tingting, S.; Yanfa, Y. *Advanced Materials* **2014**, *26*, 4653.

(42)   Shi, T.; Yin, W.-J.; Hong, F.; Zhu, K.; Yan, Y. *Applied Physics Letters* **2015**, *106*, 103902.

(43)   Buin, A.; Pietsch, P.; Xu, J.; Voznyy, O.; Ip, A. H.; Comin, R.; Sargent, E. H. *Nano Letters* **2014**, *14*, 6281.

(44)   Abate, A.; Saliba, M.; Hollman, D. J.; Stranks, S. D.; Wojciechowski, K.; Avolio, R.; Grancini, G.; Petrozza, A.; Snaith, H. J. *Nano Letters* **2014**, *14*, 3247.

(45)   Noel, N. K.; Abate, A.; Stranks, S. D.; Parrott, E. S.; Burlakov, V. M.; Goriely, A.; Snaith, H. J. *ACS Nano* **2014**, *8*, 9815.

(46)   Xu, J.; Buin, A.; Ip, A. H.; Li, W.; Voznyy, O.; Comin, R.; Yuan, M.; Jeon, S.; Ning, Z.; McDowell, J. J. *Nature Communications* **2015**, *6*, 7081.

(47)   Bhattacharjee, U.; Freppon, D.; Men, L.; Vela, J.; Smith, E. A.; Petrich, J. W. *ChemPhysChem* **2017**.

(48)   Grabolle, M.; Spieles, M.; Lesnyak, V.; Gaponik, N.; Eychmüller, A.; Resch-Genger, U. *Analytical Chemistry* **2009**, *81*, 6285.

(49)   Schmidt, L. C.; Pertegás, A.; González-Carrero, S.; Malinkiewicz, O.; Agouram, S.; Mínguez Espallargas, G.; Bolink, H. J.; Galian, R. E.; Pérez-Prieto, J. *Journal of the American Chemical Society* **2014**, *136*, 850.

(50)   De Roo, J.; Ibáñez, M.; Geiregat, P.; Nedelcu, G.; Walravens, W.; Maes, J.; Martins, J. C.; Van Driessche, I.; Kovalenko, M. V.; Hens, Z. *ACS Nano* **2016**, *10*, 2071.

(51)   Yoon, S. J.; Stamplecoskie, K. G.; Kamat, P. V. *The Journal of Physical Chemistry Letters* **2016**, *7*, 1368.

(52)   Rosales, B. A.; Hanrahan, M. P.; Boote, B. W.; Rossini, A. J.; Smith, E. A.; Vela, J. *ACS Energy Letters* **2017**, *2*, 906.

(53)   Fedeli, P.; Gazza, F.; Calestani, D.; Ferro, P.; Besagni, T.; Zappettini, A.; Calestani, G.; Marchi, E.; Ceroni, P.; Mosca, R. *The Journal of Physical Chemistry C* **2015**, *119*, 21304.

(54)   Tanaka, K.; Takahashi, T.; Ban, T.; Kondo, T.; Uchida, K.; Miura, N. *Solid State Communications* **2003**, *127*, 619.

(55)   Pellet, N.; Teuscher, J.; Maier, J.; Grätzel, M. *Chemistry of Materials* **2015**.

(56)   Stranks, S. D.; Eperon, G. E.; Grancini, G.; Menelaou, C.; Alcocer, M. J. P.; Leijtens, T.; Herz, L. M.; Petrozza, A.; Snaith, H. J. *Science* **2013**, *342*, 341.

(57)   Freppon, D. J.; Men, L.; Burkhow, S. J.; Petrich, J. W.; Vela, J.; Smith, E. A. *Journal of Materials Chemistry C* **2017**.

(58)   Hu, F.; Yin, C.; Zhang, H.; Sun, C.; Yu, W. W.; Zhang, C.; Wang, X.; Zhang, Y.; Xiao, M. *Nano Letters* **2016**, *16*, 6425.

(59)   Raino, G.; Nedelcu, G.; Protesescu, L.; Bodnarchuk, M. I.; Kovalenko, M. V.; Mahrt, R. F.; Stöferle, T. *ACS nano* **2016**.

CHAPTER 3. PHOTOPHYSICAL PROPERTIES OF WAVELENGTH-TUNABLE METHYLAMMONIUM LEAD HALIDE PEROVSKITE NANOCRYSTALS

Modified from a manuscript published in Journal of Material Chemistry C, RSC (2016);

reproduced with permission.

Daniel J. Freppon[1,2], Long Men[1,2], Sadie J. Burkhow[1,2], Jacob W. Petrich[1,2], Javier Vela[1,2], Emily A. Smith[1,2,*]

[1]Department of Chemistry, Iowa State University, and [2]Ames Laboratory, Ames, Iowa 50011

*Corresponding Authors email: esmith1@iastate.edu, vela@iastate.edu

Abstract

We present the time-correlated luminescence of isolated nanocrystals of five methylammonium lead mixed-halide perovskite compositions ($CH_3NH_3PbBr_{3-x}I_x$) that were synthesized with varying iodide and bromide anion loading. All analyzed nanocrystals had a spherical morphology with diameters in the range of 2 to 32 nm. The luminescence maxima of $CH_3NH_3PbBr_{3-x}I_x$ nanocrystals were tuned to wavelengths ranging between 498 and 740 nm by varying the halide loading. Both $CH_3NH_3PbI_3$ and $CH_3NH_3PbBr_3$ nanocrystals exhibited no luminescence intermittency for more than 90% of the 250 s analysis time, as defined by a luminescence intensity three standard deviations above the background. The mixed halide $CH_3NH_3PbBr_{0.75}I_{0.25}$, $CH_3NH_3PbBr_{0.50}I_{0.50}$, and $CH_3NH_3PbBr_{0.25}I_{0.75}$ nanocrystals exhibited luminescence intermittency in 18%, 4% and 26% of the nanocrystals, respectively. Irrespective of luminescence intermittency, luminescence intensities were classified for each nanocrystal as: (a) constant, (b) multimodal, (c) photo brightening, and (d) photobleaching. Based on their photo physics, the $CH_3NH_3PbBr_{3-x}I_x$ nanocrystals can be expected to be useful in a wide-range of

applications where low and non-intermittent luminescence is desirable, for example as imaging probes and in films for energy conversion devices.

3.1 Introduction

Luminescent semiconductors are used in a variety of applications from microscopy probes[1-4] to thin film energy capture and conversion devices.[5-19] There is increasing interest in methylammonium lead halide perovskite ($CH_3NH_3PbX_3$, X= halide) materials due to their low cost, broad absorption as well as their charge transport diffusion lengths that range from ~100 nm to greater than 175 µm.[20-24] In energy capture and conversion films, large exciton diffusion lengths remove the need for a transport layer in perovskite-based solar cells, thus simplifying the device architecture. Single-crystalline nanocrystals, as opposed to polycrystalline films, could increase the efficiency of energy capture and conversion devices. $CH_3NH_3PbX_3$ nanocrystals are also being evaluated for use in light emitting diodes,[25] and as lasing materials.[26]

Organometal halide perovskites do exhibit photostability issues.[27,28] Specifically, perovskites degrade upon exposure to light over time.[29,30] Further, Matsumoto et al. and Manshor et al. both report noticeable degradation of $CH_3NH_3PbI_3$ to PbI_2 when exposed to both light and humidity, but claim it remains stable when exposed to photon dose only.[31,32] Superoxide (O^{2-}), generated from photoreaction of perovskites and oxygen, can also accelerate the degradation process to PbI_2, I_2 and CH_3NH_2.[33] The mechanism of photo degradation is still under debate, so it is important to study luminescence intermittency to better understand the photo-physics and phot-chemistry of perovskites.

When illuminated with visible light, many types of semiconductor materials show luminescence intermittency (*i.e.*, blinking), a luminescence intensity that drops below the background or other threshold intensity.[34-48] In addition to the energy capture and conversion

applications outlined above, there are many uses for non-intermittent, photostable, as well as tunable nanocrystals. For example, as imaging probes the nanocrystal absorption and emission wavelengths should match wavelength criteria for the optical setup, so tunability is advantageous. Tuning the luminescence wavelength of $CsPbX_3$[49-51] as well as $CH_3NH_3PbX_3$[52-55] perovskite nanocrystals across the visible spectrum has been reported.

The photostability of $CH_3NH_3PbX_3$ nanocrystals and films has been studied by Zhu *et al.*[45] and Yuan *et al.*[56] $CH_3NH_3PbBr_3$ nanocrystals have been shown to degrade under an intense electron beam used in transmission electron microscopy.[45] Laser illumination with 500 W/cm^2 was shown to cause photodamage to $CH_3NH_3PbI_3$ films within several seconds, leading to a decrease in luminescence.[56] Whereas, little photobleaching (*i.e.*, decreasing luminescence) or photo brightening (*i.e.*, increasing luminescence) was observed for $CH_3NH_3PbI_3$ nanocrystals with wire, rod, and dot morphologies using mercury lamp illumination.[45]

In addition to photostability, luminescence intermittency has also been reported for $CH_3NH_3PbX_3$ materials,[19,41,42,45,46,112,114] although the mechanism is still under debate.[34-35, 38-39] One reported mechanism of luminescence intermittency in a dense $CH_3NH_3PbBr_3$ nanocrystal film is non-radiative Auger-like recombination of electrons and holes due to the accumulation of charge.[42] In closely packed nanocrystals, charge accumulates at the surface and nanocrystal interface leading to intermittency; whereas, no intermittency is measured for well-dispersed nanocrystals. On the other hand, Tachikawa *et al.* report intermittency in single $CH_3NH_3PbBr_3$ nanocrystals and postulate it is the result of charge trapping by surface Pb sites reducing the probability of a recombination event.[46] They estimate 1 to 4 trap sites per 10 to 50-nm nanocrystal. The halide composition affects the trap density; an order of magnitude lower trap site density is measured in $CH_3NH_3PbI_3$ films grown in the presence of chloride compared to

films in the absence of chloride.[57] In a $CH_3NH_3PbI_3$ film, a deep trap state 0.16 eV above the valence band has been measured, and calculations show this trap might arise from iodine defects.[58]

Zheng *et al.* report the differences in bulk crystals and nanocrystals of $CH_3NH_3PbBr_3$.[59] In bulk $CH_3NH_3PbBr_3$, filling of trap sites is dependent on the photon density, and luminescence lifetimes increase with higher photon densities. Compared to bulk, the luminescence lifetime of $CH_3NH_3PbBr_3$ nanocrystals is not as dependent on photon densities; 30% of the excitation photons undergo trap-free recombination; trap states are more likely to be present on the surface than in the volume of the crystal; and trap lifetimes can be short. Tian *et al.* have shown that light illumination removes traps leading to photo brightening in $CH_3NH_3PbI_3$ films, and that the size of $CH_3NH_3PbI_3$ crystallites (nanometers to microns) within the film has an effect on the rate of photo brightening.[60]

Here, we report the data from three luminescence techniques used to measure the photo physics of $CH_3NH_3PbBr_{3-x}I_x$ nanocrystals to gain a fundamental understanding of how composition affects their luminescence and, thus, their continued and potential usability in energy conversion and imaging applications. Ensemble luminescence measurements show the nanocrystal emission wavelengths are tunable across the visible wavelength region by varying the ratio of iodide and bromide salts in the synthetic loading. Due to heterogeneous crystal formation, individual nanocrystal photophysical properties vary with the type and number of defect and trap sites. Nanocrystal microscopy measures the luminescence intensity over time to reveal the temporal dynamics (*e.g.*, intermittency, flickering) as well as heterogeneity in the photophysical properties. Finally, nanocrystal micro spectroscopy enables the full luminescence

spectrum of isolated nanocrystals to be collected in order to monitor the stability of the emission peak over time.

3.2 Experimental

3.2.1 Materials

Lead(II) iodide (PbI_2, 99%), lead(II) bromide ($PbBr_2$, ≥98%), methylamine (CH_3NH_2, 33 wt% in ethanol), N,N-dimethylformamide (DMF, 99.8%, anhydrous) and n-octylamine ($CH_3(CH_2)_7NH_2$, 99%) were purchased from Sigma-Aldrich; hydroiodic acid (ACS, 55-58%) and hydrobromic acid (ACS, 47.0-49.0%) from Alfa-Aesar; acetonitrile (99.9%) and toluene (99.9%) from Fisher Scientific. All chemicals were used as received.

3.2.2 Synthesis of Methylammonium Lead (II) Mixed-halide Nanocrystals

Precursor solutions. Alkylammonium halides were prepared by a slightly modified literature procedure.[53] Briefly, hydroiodic acid (10 mL, 0.075 mol) or hydrobromic acid (8.6 mL, 0.075 mol) was added to a solution of excess methylamine (24 mL, 0.19 mol) or *n*-octylamine (32 mL, 0.19 mol) in ethanol (100 mL) at 0 °C, and the mixture stirred at 0 °C for 2 h. The sample was concentrated under vacuum, first in a rotary evaporator at 70 °C, and then under dynamic vacuum at 60 °C for 12 h. The remaining solid was recrystallized from ethanol. *Br Solution.* $PbBr_2$ (2.9 mg, 0.008 mmol), CH_3NH_3Br (1.3 mg, 0.012 mmol) and $CH_3(CH_2)_7NH_3Br$ (2.5 mg, 0.012 mmol) were dissolved in a mixture of acetonitrile (20 mL) and DMF (0.2 mL). *I Solution.* PbI_2 (3.7 mg, 0.008 mmol), CH_3NH_3I (1.9 mg, 0.012 mmol) and $CH_3(CH_2)_7NH_3I$ (3.1 mg, 0.012 mmol) were dissolved in a mixture of acetonitrile (20 mL) and DMF (0.2 mL). *CH_3NH_3Pb (Br_xI_{1-x})$_3$ nanocrystals.* Portions of *Br* and *I* solutions were mixed according to the different desired halide loadings to a total volume of 4 mL, followed by the rapid addition of toluene (15 mL) while stirring. After 24 h stirring at room temperature, solids were isolated by

centrifugation (5 min at 4500 rpm) and washed with toluene (5 mL). Solids were suspended into 10 mL toluene which resulted in a nanocrystal concentration of approximately 1 mM.

3.3.3 Nanocrystal Ensemble Characterization

XRD was measured using Cu Kα radiation on a Rigaku Ultima diffractometer. Solution extinction (absorption plus scattering) spectra were measured with a photodiode array Agilent 8453 UV-Vis spectrophotometer. Steady-state PL spectra were measured using a Horiba-Jobin Yvon Nanolog scanning spectrofluorometer. Relative PL quantum yields (QYs) were measured following literature procedures, using either Rhodamine 590 or Rhodamine 640 dye as a standard.[61] Absorption and PL emission spectra were measured as duplicates and the average QYs were recorded.

3.3.4 Nanocrystal Luminescence Microscopy

$CH_3NH_3PbBr_{3-x}I_x$ nanocrystals prepared from precursor solutions using the method stated earlier were diluted to a tenth (/10) in toluene (~0.3 mM, 50 µL) and sonicated for 90 minutes before drop casting onto a glass microscope coverslip (Carlson Scientific, Peotone, IL, USA). Nanocrystal luminescence microscopy was performed using an upright microscope (Nikon Eclipse 80i, Melville, NY, USA). A mercury lamp was used for excitation (XCite 120 PC, EXFO Photonic Solutions Inc., Quebec City, Canada). Excitation and emission filters were from Omega Optical (Brattleboro, VT, USA), unless noted otherwise: 500 ± 5 nm excitation and 535 ± 7.5 nm emission filters were used for the $CH_3NH_3PbBr_3$, $CH_3NH_3Pb(Br_{0.75}I_{0.25})_3$, and $CH_3NH_3Pb(Br_{0.50}I_{0.50})_3$ samples; 500 ± 5 nm excitation and 615 ± 15 nm emission filters were used for the $CH_3NH_3Pb(Br_{0.25}I_{0.75})_3$ sample; 510 ± 5 nm excitation and 730 ± 40 nm emission filters (Semrock, Inc., Lake Forest, IL, USA) were used for the $CH3NH_3PbI_3$ sample. A 100× PlanApo, 1.49 numerical aperture oil-immersion objective was used and *photoluminescence (PL)*

images were collected in the epi-direction using a charged-coupled device (CCD) camera (Photometrics Evolve, Tucson, AZ, USA) with a 250 millisecond exposure time and zero gain. Each PL movie consists of 1000 images/frames collected sequentially for a total analysis time of 250 seconds. The signal-to-noise ratio was at least 2 at the start of each movie, and a diffraction-limited point spread function was measured for each analyzed nanocrystal.

3.3.5 Threshold Calculation

ImageJ was used to analyze the PL movies. For each nanocrystal analyzed, the nanocrystal's luminescence intensity and a background value were quantified in each of the 1000 frames using the Z-axis Profile function in ImageJ. The most intense pixel for the spheroid nanocrystals was used to plot the nanocrystal luminescence intensity over the entire 1000 frames (*i.e.*, over time). The background in each frame was measured approximately 8 pixels away from the center of each nanocrystal. The average background value (μ_{bg}) and background standard deviation (σ_{bg}) were calculated across all 1000 frames, and was used to calculate a threshold: Threshold = $\mu_{bg} + 3\sigma_{bg}$. Nanocrystals were considered intermittent in luminescence if their intensity fell below the threshold for more than 25 seconds over the entire movie (*i.e.*, 10% of the collection time).

3.3.6 Nanocrystal Microspectroscopy

The suspended $CH_3NH_3Pb(Br_{0.75}I_{0.25})_3$ nanocrystals prepared from precursor were diluted to a tenth (/10) in toluene (~0.3 mM, 50 μL) and sonicated for 60 min before drop casting onto a glass microscope coverslip (Carlson Scientific, Peotone, IL). A lab-built optical microscope based on a DM IRBE platform (Leica, Wetzlar, Germany) with 532-nm laser excitation (Sapphire SF 532 nm, Coherent, Santa Clara, CA, USA) was used to collect *emission spectra* as a function of illumination time. A 100× HCX PL APO, 1.49 numerical aperture oil-immersion

objective (Leica) was used to achieve a laser spot with a diameter of 440 nm. The excitation power density at the sample was 1×10^5 W/cm^2. Photoluminescence was collected from the epi-direction and focused onto a HoloSpec f/1.8i spectrograph (Kaiser Optical Systems, Ann Arbor, MI, USA) equipped with a broad range grating (HFG-650, Kaiser Optical Systems) and then directed to a CCD (Newton 940, Andor Technology, Belfast, UK). A series of 2500 spectra were collected for 0.1 second each. Spectra were then analyzed using IGOR Pro 6.34 batch fit (Wavemetrics, Lake Oswego, OR) and 3D images of the fits shown in Figure 5 were plotted in Matlab 2016a (Mathworks, Natick, MA).

3.4 Results and Discussion

Five $CH_3NH_3PbBr_{3-x}I_x$ nanocrystal compositions were prepared with $X = 0$, 0.75, 1.50, 2.25 and 3. Throughout, the presented formulas refer to the synthetic loading not a measured nanocrystal composition. All synthetic loadings produced primarily spherical nanocrystals, as shown by transmission electron microscopy (Fig. S3.1). The XRD pattern shows a major peak at 30.2 degrees for $CH_3NH_3PbBr_3$ nanocrystals, which corresponds to a cubic crystal structure, and a peak at 28.7 for $CH_3NH_3PbI_3$ nanocrystals, which corresponds to a tetragonal crystal structure (Fig. S3.2). The mixed halide perovskites we studied are nanocrystalline. To control particle size, we used octyl ammonium halides ($CH_3(CH_2)_7NH_3X$) as surfactants, which we have shown passivate the surface and terminate/truncate further crystal growth. The experimental XRD patterns of $CH_3NH_3PbI_3$ and $CH_3NH_3PbBr_3$ indicate the nanocrystals grow mainly along the [110] direction.[45] This preferred orientation is the main reason behind the differences observed between the experimental and standard XRD patterns, which were collected from bulk single crystals.

According to the experimental patterns of $CH_3NH_3PbBr_{3-x}I_x$ (x=0.25, 0.50, 0.75), all three crystal structures are cubic, because only one diffraction peak is shown around 15 2θ degree, which is corresponding to (001) plane of cubic structure. Our observation is also consistent with Zhu *et al.*[45]

The $CH_3NH_3PbBr_{3-x}I_x$ nanocrystals absorbed a broad range of visible wavelengths (Fig. 3.1). The luminescence spectra show a range in their wavelength of maximum emission with halide loading (Fig.3.1). As the iodide content increased from 0 ($CH_3NH_3PbBr_3$) to 100% ($CH_3NH_3PbI_3$), the luminescence maximum shifted from 498 to 740 nm. The shift in luminescence maximum is not linear with halide loading (Fig.3.2), which is consistent with previous reports.[52,62]
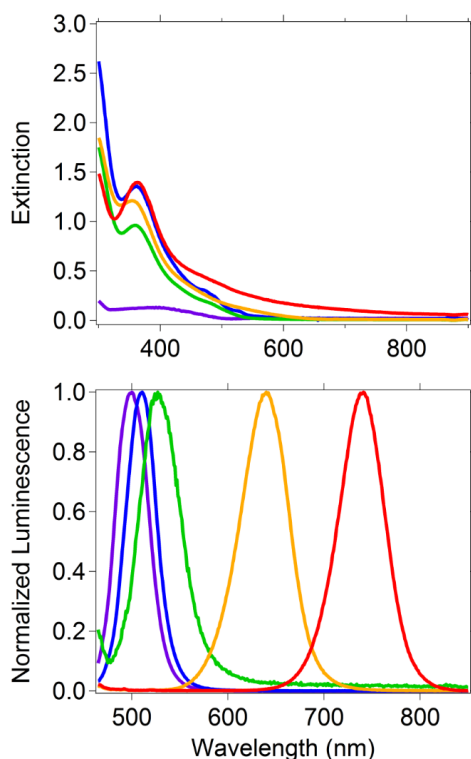
Fig 3.1. (Top) Extinction (absorption plus scattering) and (bottom) normalized emission with 375 nm excitation spectra of $CH_3NH_3PbBr_3$ (purple), CH_3NH_3Pb $(Br_{0.75}I_{0.25})_3$ (blue), CH_3NH_3Pb $(Br_{0.50}I_{0.50})_3$ (green), CH_3NH_3Pb $(Br_{0.25}I_{0.75})_3$ (orange), $CH_3NH_3PbI_3$ (red). Extinction and emission spectra were collected in toluene as the solvent.

The luminescence intensity as a function of time was analyzed for up to 50 nanocrystals from each halide loading. The $CH_3NH_3(Br_{0.25}I_{0.75})_3$ nanocrystals were more dilute relative to the other compositions over replicate syntheses and the same sample preparation method only allowed 39 nanocrystals to be measured. An average luminescence intensity across the 250 second analysis time was calculated for each nanocrystal; histograms of the background subtracted values are shown in Fig. S3.3 for each halide loading. The absolute values on the x-axis cannot be compared across different compositions as the optical throughput of the instrument varies with wavelength (*e.g.*, filter bandwidth, *etc.*). The shapes of the distributions, however, can be compared. The mixed halide compositions of $CH_3NH_3Pb(Br_{0.75}I_{0.25})_3$, $CH_3NH_3Pb(Br_{0.50}I_{0.50})_3$, and $CH_3NH_3Pb(Br_{0.25}I_{0.75})_3$ had more outliers with intensities 13 to $230\times$ higher than the intensity with the highest frequency compared to the single halide $CH_3NH_3PbBr_3$ and $CH_3NH_3PbI_3$ nanocrystals.
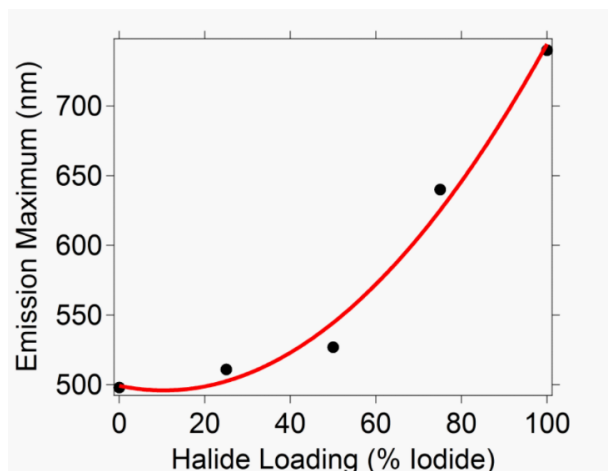
Fig 3.2. Emission maximum wavelength versus iodide loading for the (0%) $CH_3NH_3PbBr_3$, (25%) $CH_3NH_3Pb(Br_{0.75}I_{0.25})_3$, (50%) $CH_3NH_3Pb(Br_{0.50}I_{0.50})_3$, (75%) $CH_3NH_3Pb(Br_{0.25}I_{0.75})_3$, and (100%) $CH_3NH_3PbI_3$ nanocrystals. The third-order polynomial fit line is shown in red. The equation for the best fit of the maximum emission wavelength (λ_{max}) versus percent iodide loading (x) is: $\lambda_{max} = -9 \times 10^{-5}x^3 + 0.04x^2 - x + 501$. The R^2 value for the fit is 0.99.

The single halide nanocrystals exhibit no luminescence intermittency as defined by a luminescence intensity above the calculated threshold for distinguishing luminescence from the background more than 90% of the analysis time (Table 3.1). The percentage of CH_3NH_3Pb $(Br_{0.75}I_{0.25})_3$, CH_3NH_3Pb $(Br_{0.50}I_{0.50})_3$, and CH_3NH_3Pb $(Br_{0.25}I_{0.75})_3$ nanocrystals that exhibit luminescence intermittency is 18, 4, and 26%, respectively. We hypothesize that the fraction of mixed halide nanocrystals that exhibit intermittency due to crystal defects or trap states. The single halide perovskites, $CH_3NH_3PbI_3$ and $CH_3NH_3PbBr_3$, have quantum yields of 1.5% and 44% respectively. These quantum yields are higher than the mixed halide perovskite nanocrystals (0.02 to 1.3%), which is consistent with the hypothesis that increased crystal defects or trap states are responsible for blinking in the mixed halide perovskites. It is likely that I or Br incorporation into a crystal is unlikely to form a homogenous lattice when the synthesis has a higher loading of one halide compared to the other. Compared to $CH_3NH_3PbI_3$, $CH_3NH_3PbBr_3$ perovskites have a lower relative reaction enthalpy, providing to more stability in thin films.[63] Additional work to probe this issue is under way. When electrons become trapped, luminescent recombination of excitons cannot occur, providing periods of no measured luminescence. Further, this leads to the assumption that functional trap states are absent in the single halide nanocrystals.

Table 3.1. Percentage of nanocrystals within each composition that are above the calculated threshold over 90% of the analysis time (*i.e.*, "ON") and the percentage of time the nanocrystals are above the threshold.

a The nanocrystals are in an "ON" state if the luminescence intensity is above the calculated threshold at least 90% of the analysis time.

b Based on a total time of 250 seconds × number of nanocrystals analyzed.

Sample	Number of Nanocrystals Analyzed	Percentage **Nanocrystals** "ON"[a]	Percentage **Time** Above Threshold[b]
$CH_3NH_3PbBr_3$	50	100	100
$CH_3NH_3Pb(Br_{0.75}I_{0.25})_3$	50	82	93
$CH_3NH_3Pb(Br_{0.50}I_{0.50})_3$	50	96	99
$CH_3NH_3Pb(Br_{0.25}I_{0.75})_3$	39	74	89
$CH_3NH_3PbI_3$	50	100	100

In addition to the percentage of nanocrystals that exhibit intermittency, it is also useful to consider the percentage of time the nanocrystals were above the threshold over the total analysis time (Table 3.1). The intensities of the $CH_3NH_3PbBr_3$ and $CH_3NH_3PbI_3$ nanocrystals are always above the threshold over the entire 208 minutes (*i.e.*, 50 nanocrystals analyzed for 250 seconds each). For the intermediate halide loadings, the percentage of non-intermittent nanocrystals and the percentage of the analysis time the nanocrystals are above the threshold are correlated. The latter, however, is always higher than the former. For example, 74% of the CH_3NH_3Pb $(Br_{0.25}I_{0.75})_3$ nanocrystals are not intermittent and are above the threshold 89% of the analysis time.

The luminescence signal over time was categorized into four different luminescence behaviors irrespective of the threshold or intermittency (Table 3.2). The behaviors are: (a) constant intensity, (b) multimodal intensity, (c) photo brightening, and (d) photobleaching. In order to be classified as constant luminescence intensity, shown in Fig. 3.3a, the slope of the line connecting the intensity at 0 seconds and 250 seconds was between -0.2 and 0.2 s^{-1}. The small fluctuations in intensity of a nanocrystal classified as constant luminescence are due to

instrument noise; this produces an intensity histogram with a Gaussian distribution (Fig. 3.3a').

The CH_3NH_3Pb $(Br_{0.75}I_{0.25})_3$ and CH_3NH_3Pb $(Br_{0.50}I_{0.50})_3$ nanocrystals were the only

compositions to exhibit type a constant intensity with populations of 28% for both compositions

(Table 3.2).

Table 3.2. Number of nanocrystals analyzed for each halide loading and percentage that display type a, b, c, and d photoluminescence as defined in the text.

Sample	Number of Nanocrystals Analyzed	Type a: Constant Intensity	Type b: Multimodal Intensity Profile	Type c: Photo-brightening	Type d: Photo-bleaching
$CH_3NH_3PbBr_3$	50	0%	70%	4%	26%
$CH_3NH_3Pb(Br_{0.75}I_{0.25})_3$	50	28%	38%	22%	12%
$CH_3NH_3Pb(Br_{0.50}I_{0.50})_3$	50	28%	18%	8%	46%
$CH_3NH_3Pb(Br_{0.25}I_{0.75})_3$	39	0%	0%	5%	95%
$CH_3NH_3PbI_3$	50	0%	18%	8%	74%

If the intensity of a nanocrystal varied between two or three relatively constant values for

a duration of at least 10 seconds with the transition between intensities occurring within 500

millisecond (*i.e.*, two times the acquisition time), this is classified as type b multimodal behavior,

shown in Fig. 3.3b. The resulting intensity histogram is either a bimodal or trimodal distribution

(Fig. 3.3b'). The number of nanocrystals that have a multimodal intensity profile decreased with

the amount of bromide loading from $CH_3NH_3PbBr_3$ to CH_3NH_3Pb $(Br_{0.25}I_{0.75})$. The $CH_3NH_3PbI_3$

nanocrystals do not fit this trend with 18% of nanocrystals exhibiting this behavior. Across all

nanocrystal compositions, 72 exhibited multimodal behavior, and this was the second most

common behavior. Eight of the 72 total where trimodal (only found in the $CH_3NH_3PbBr_3$ and

CH_3NH_3Pb $(Br_{0.75}I_{0.25})_3$ compositions) and 64 were bimodal. A possible mechanism for type b

photo physics is considered: Given the nanocrystals are smaller than the diffraction limit of light, it is possible that a bimodal luminescence intensity is from nanocrystal dimers or aggregates. Considering a bimodal distribution, the most common type b behavior, and a possible nanocrystal dimer, the high luminescence state would represent times when both nanocrystals are emitting; whereas, the low intensity state would represent times when only one nanocrystal is emitting. Statistically, there is a possibility that both nanocrystals are not emitting, and the intensity would drop below the threshold. This possibility increases as the duration of the low intensity state increases; however, an intensity below the threshold is never measured in this population. One may argue that the lower intensity state is one where the nanocrystal is not luminescent, and that an incorrect threshold has been applied. However, the image inset in Fig. 3.3b clearly show that the low intensity state is higher than the background. A low intensity, or gray state, has been reported for quantum dots, including ZnS capped CdSe[64] and CdS capped CdSe.[65,66] The emitting low intensity state in $CH_3NH_3PbBr_{3-x}I_x$ nanocrystals may be a gray state, although the mechanism for the gray state may be unique and requires further study.
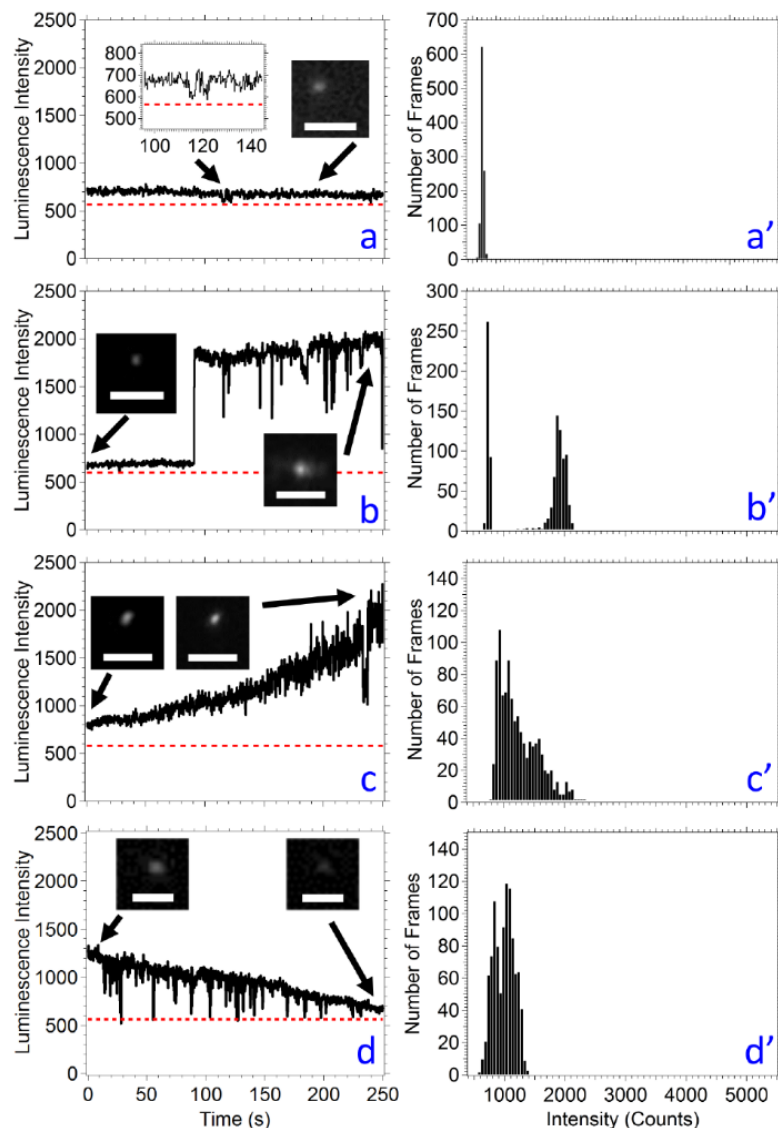
Fig 3.3. Representative luminescence intensity versus time graphs for $CH_3NH_3Pb (Br_{0.75}I_{0.25})_3$ nanocrystals. The dotted red line is the threshold for distinguishing nanocrystal luminescence from the background. The panels represent four of the photophysical properties measured for all the perovskite compositions. The time-correlated luminescence intensity is found on the left. Histograms of the corresponding intensities are found on the right. Type (a) is representative of nanocrystals that only show fluctuations in luminescence intensity due to instrument noise. Type (b) is representative of nanocrystals that exhibit a multimodal luminescence intensity profile, in this case being bimodal, a low intensity and a high intensity or vice versa. Type (c) is representative of nanocrystals with luminescence intensities that photo brighten over time (a slope greater than 0.2 s^{-1}). Type (d) is representative of nanocrystals with luminescence intensities that photo bleach over time (a slope smaller than -0.2 s^{-1}). Figures on the right show the intensity histograms for all 250 seconds. Each histogram corresponds to the similar letter (*e.g.* a' corresponds to a). The insets show the image at selected time points, as noted by the arrow. In all cases, the images show a nanocrystal intensity that can be differentiated from the background. The scale bar in each image is 2 μm and the acquisition time is 250 millisecond.

In up to 22% of the population, the luminescence intensity of a nanocrystal increased over the analysis time. If the slope of the intensity between the data points at time 0 seconds and 250 seconds was greater than 0.2 s^{-1}, then the nanocrystal was photo brightening, shown in Fig. 3.3c. Photo brightening results in an intensity histogram with an asymmetric distribution (Figure 3c'). In the case of Fig. 3.3c, and whenever there is photo brightening, a skew does exist towards higher intensities. Photo brightening has been reported in $CH_3NH_3PbBr_3$ nanocrystals and $CH_3NH_3PbI_3$ films by Tachikawa *et al.* and deQuilettes *et al.*, respectively.[46,67] One mechanism reported for photo brightening is a photoinduced trap reduction caused by the movement of halides when illuminated with light. As the halides are transported about the nanocrystalline lattice, vacancies that make up trap sites are filled. Considering all nanocrystal compositions as an aggregate, this is the least common behavior.

Each nanocrystal composition produced a population where the luminescence intensity of a nanocrystal decreased over the analysis time. If the slope of the intensity between the data points at time 0 seconds and 250 seconds was less than -0.2 s^{-1}, then the nanocrystal was considered to be photobleaching, shown in Fig. 3.3d. Photobleaching generally results in an intensity histogram that skews to lower values (Fig. 3.3d'). Photobleaching was most common (74-95%) in the nanocrystals containing high amounts of iodide (*i.e.*, $CH_3NH_3Pb(Br_{0.25}I_{0.75})_3$ and $CH_3NH_3PbI_3$). We hypothesize that in cases of photobleaching, the nanocrystal lattice begins to decompose leading to higher non-radiative recombination events, which has also been observed in $CsPbX_3$ nanocrystals[43] and CdSe/ZnS quantum dots.[68] A small number of nanocrystals exhibited photobleaching as well as short periods of lower intensity up to 10 s in duration (*i.e.*, below the 50 seconds used to categorize a nanocrystal as exhibiting a bimodal

distribution). Each nanocrystal was analyzed for 250 seconds; it is possible that the percentage of nanocrystals with type d photobleaching behavior increases as the analysis time increases.

Flickering is defined here as less than 500 millisecond (*i.e.*, two times the acquisition time) periods of a drop in luminescence intensity. Flickering is observed in types b, c, and d luminescence behaviors. Examples of flickering are shown in Fig. 3.3b and d. In some instances of flickering, the luminescence intensity goes below the threshold, which represent brief intermittent events. For the events that do not go below the threshold, a faster acquisition rate may reveal whether these events represent intermittent events. A faster acquisition time of 20 millisecond was used to measure the time correlated luminescence intensity of all nanocrystal compositions; results for one composition are shown in Fig. 3.4 and for the other compositions in Fig. S3.4. Most of the flickering measured with a 20-millisecond acquisition time remain above the threshold, revealing a mechanism faster than 20 milliseconds is responsible for most of these events.
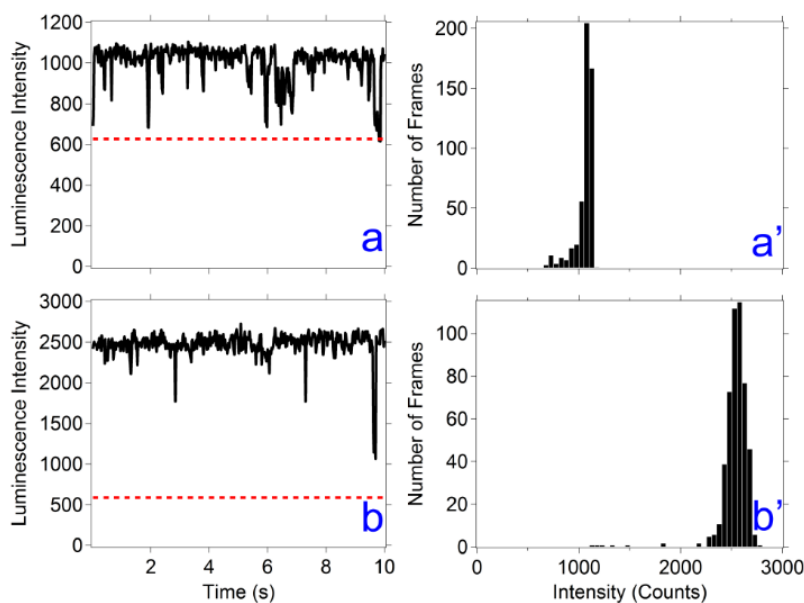
Fig 3.4. Representative luminescence intensity versus time graphs for $CH_3NH_3PbBr_3$ nanocrystals. The acquisition time is 20 millisecond, collected over 10 seconds. The dotted red line is the threshold for distinguishing nanocrystal luminescence from the background.

In the nanocrystal luminescence microscopy experiments described above, increasing, decreasing or flickering luminescence could be explained by shifting luminescence spectra, which has been measured in similar nanocrystals.[69] If the luminescence shifts partially, or completely, outside the wavelength range of the filters used to collect the signal, then the luminescence intensity could increase, decrease, or disappear. In order to test for this, the emission spectrum of isolated $CH_3NH_3PbI_3$ nanocrystals was measured over 250 seconds under 1 $\times 10^5$ W/cm^2 laser irradiance (Fig. 3.5). The emission maximum remained constant at 775 nm under continuous illumination with a 100 millisecond acquisition time. The emission does not shift outside the wavelength region of the filters used to collect the luminescence intensity versus time data. This indicates that the blinking or other varying luminescence intensity states measured for the $CH_3NH_3PbI_3$ nanocrystals (Table 3.1) is not the result of shifting luminescence spectra. The instrument setup does not allow the measurement of the other nanocrystal compositions. Finally, this experiment shows that 50% of the nanocrystal exhibit photo brightening and 50% photobleaching under high irradiance, and overall better photostability than many reported in the literature for similar materials.[43,70]
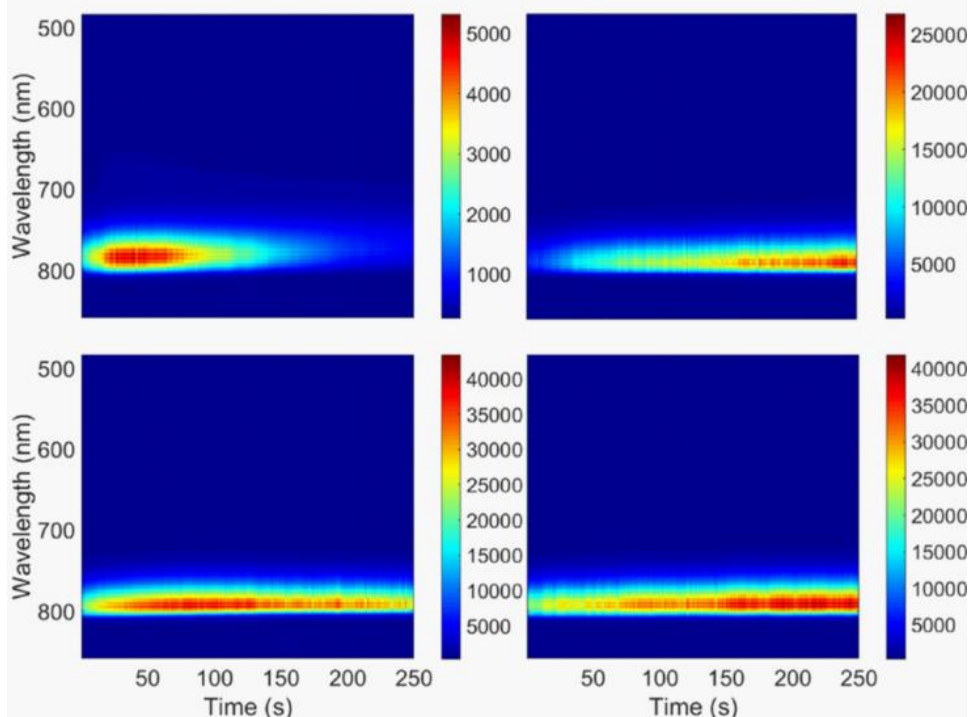
Fig 3.5. Luminescence spectra of $CH_3NH_3PbI_3$ nanocrystals over time. Each panel represents a different nanocrystal. The luminescence maximum is constant over time at 775 nm. (This is shifted relative to the ensemble solution data shown in Fig. 3.1). The excitation wavelength is 532 nm; the acquisition time is 0.1 seconds.

3.5 Conclusion

The nanocrystal luminescence analysis of a series of methylammonium lead halide nanocrystals has been reported. The wavelength of maximum luminescence was tunable within the range of 498-740 nm by controlling the bromide and iodide loading during nanocrystal synthesis. The $CH_3NH_3PbI_3$ and $CH_3NH_3PbBr_3$ nanocrystals exhibit no luminescence intermittency, while 82%, 96%, and 74% of the $CH_3NH_3Pb(Br_{0.75}I_{0.25})_3$, $CH_3NH_3Pb(Br_{0.50}I_{0.50})_3$, and $CH_3NH_3Pb(Br_{0.25}I_{0.75})_3$ nanocrystals exhibit no luminescence intermittency, respectively. The low percentage of nanocrystals which exhibited intermittency, along with relatively good photo stabilities at low (*i.e.*, mercury lamp) and high (*i.e.*, focused laser, up to 1×10^5 W/cm^2) photon fluxes, and the emission tunability of the nanocrystals, this specific synthesis method can

provide hybrid perovskite nanocrystals which will be useful in a wide range of luminescence and microscopy techniques.

3.6 Acknowledgements

Chapter 3 Supplemental Information

Transmission Electron Microscopy

Transmission Electron Microscopy (TEM). TEM was conducted using a FEI Technai G2 F20 field emission TEM operating at up to 200 kV with a point-to-point resolution of less than 0.25 nm and a line-to-line resolution of less than 0.10 nm. Samples were prepared by placing 2 or 3 drops of dilute toluene solutions onto carbon-coated copper grids.

Size and Morphology Analysis. Particle dimensions were measured manually and with ImageJ. Typically, more than 100 particles were counted in each case. Uncertainties in all measurements are reported as standard deviations.
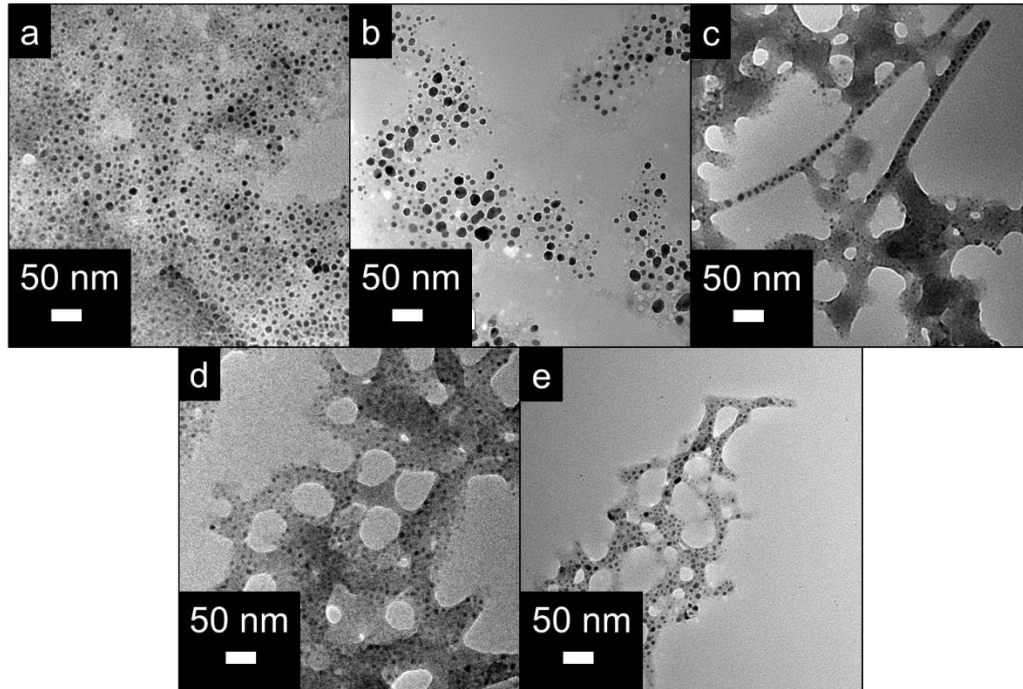
Figure S3.1. TEM images of (a) $CH_3NH_3PbBr_3$, (b) CH_3NH_3Pb $(Br_{0.75}I_{0.25})_3$, (c) CH_3NH_3Pb $(Br_{0.50}I_{0.50})_3$, (d) CH_3NH_3Pb $(Br_{0.25}I_{0.75})_3$, and (e) $CH_3NH_3PbI_3$ nanocrystals.
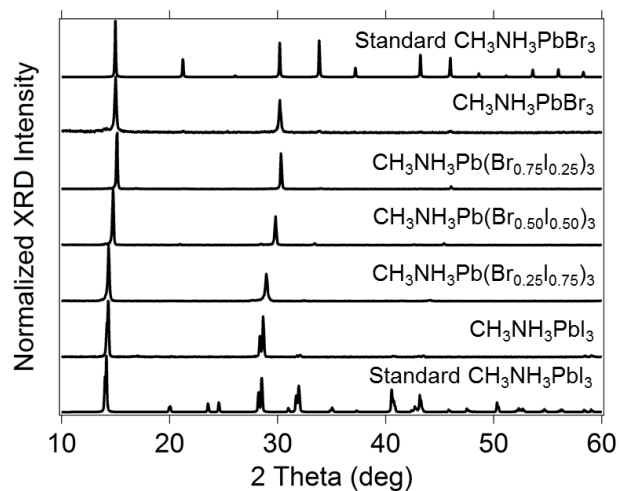
Figure S3.2. X-ray diffraction (XRD) patterns of $CH_3NH_3PbBr_3$, CH_3NH_3Pb $(Br_{0.75}I_{0.25})_3$, CH_3NH_3Pb $(Br_{0.50}I_{0.50})_3$, CH_3NH_3Pb $(Br_{0.25}I_{0.75})_3$, and $CH_3NH_3PbI_3$ nanocrystals. Also included are the standard XRD patterns for the cubic $CH_3NH_3PbBr_3$ and tetragonal $CH_3NH_3PbI_3$ crystal structures, respectively. The various halide percentages stated in the formulas represent synthetic loading rather than a measured composition of the nanocrystals.
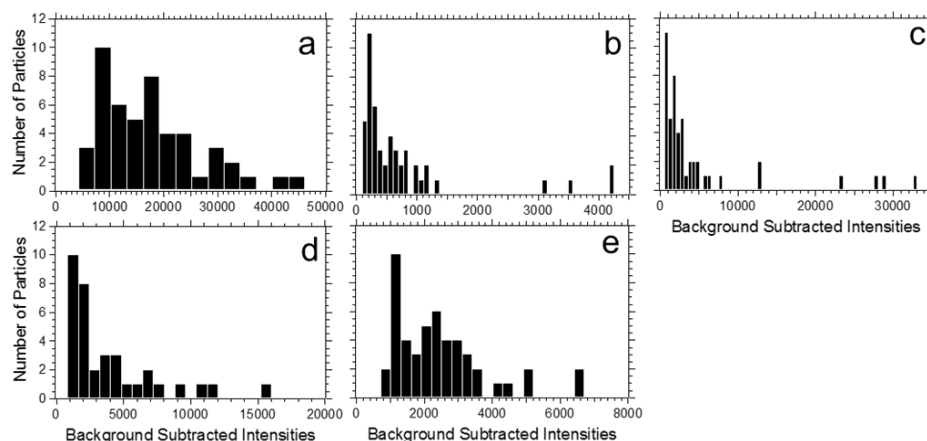
Figure S3.3. Histograms of the average background subtracted nanocrystal luminescence intensity for the perovskite compositions: (a) $CH_3NH_3PbBr_3$, (b) $CH_3NH_3Pb (Br_{0.75}I_{0.25})_3$, (c) $CH_3NH_3Pb (Br_{0.50}I_{0.50})_3$, (d) $CH_3NH_3Pb (Br_{0.25}I_{0.75})_3$, and (e) $CH_3NH_3PbI_3$. Each histogram was generated to have 10 or 11 nanocrystals as a maximum frequency, so the bin size varies among each composition. A total of 50 nanocrystals were analyzed in all cases except (d), which had 39 nanocrystals analyzed.
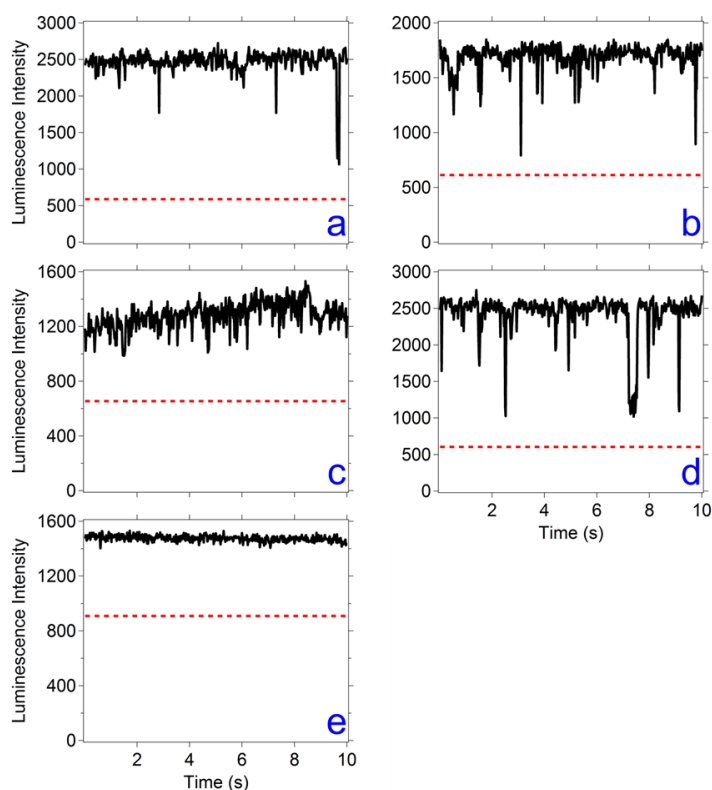
Figure S3.4. Representative luminescence intensity versus time graphs for (a) $CH_3NH_3PbBr_3$, (b) $CH_3NH_3Pb (Br_{0.75}I_{0.25})_3$, (c) $CH_3NH_3Pb (Br_{0.50}I_{0.50})_3$, (d) $CH_3NH_3Pb (Br_{0.25}I_{0.75})_3$, and (e) $CH_3NH_3PbI_3$ nanocrystals. The acquisition time is 20 ms, collected over 10 s. The dotted red line is the threshold for distinguishing nanocrystal luminescence from the background.

References

(1)   Lane, L. A.; Smith, A. M.; Lian, T.; Nie, S. *The Journal of Physical Chemistry B* **2014**, *118*, 14140.

(2)   Luo, J.; Bai, H.; Yang, P.; Cai, J. *Materials Science in Semiconductor Processing* **2015**, *34*, 1.

(3)   Fernández-Suárez, M.; Ting, A. Y. *Nature Reviews Molecular Cell Biology* **2008**, *9*, 929.

(4)   Orte, A.; Alvarez-Pez, J. M.; Ruedas-Rama, M. J. *ACS Nano* **2013**, *7*, 6387.

(5)   Patel, P.; Mitzi, D. *MRS Bulletin* **2014**, *39*, 768.

(6)   Snaith, H. J. *The Journal of Physical Chemistry Letters* **2013**, *4*, 3623.

(7)   Park, N.-G. *The Journal of Physical Chemistry Letters* **2013**, *4*, 2423.

(8)   Stranks, S. D.; Nayak, P. K.; Zhang, W.; Stergiopoulos, T.; Snaith, H. J. *Angewandte Chemie International Edition* **2015**, *54*, 3240.

(9)   Edri, E.; Kirmayer, S.; Cahen, D.; Hodes, G. *The Journal of Physical Chemistry Letters* **2013**, *4*, 897.

(10)   Edri, E.; Kirmayer, S.; Kulbak, M.; Hodes, G.; Cahen, D. *The Journal of Physical Chemistry Letters* **2014**, *5*, 429.

(11)   De Wolf, S.; Holovsky, J.; Moon, S.-J.; Löper, P.; Niesen, B.; Ledinsky, M.; Haug, F.-J.; Yum, J.-H.; Ballif, C. *The Journal of Physical Chemistry Letters* **2014**, *5*, 1035.

(12)   Unger, E. L.; Hoke, E. T.; Bailie, C. D.; Nguyen, W. H.; Bowring, A. R.; Heumuller, T.; Christoforo, M. G.; McGehee, M. D. *Energy & Environmental Science* **2014**, *7*, 3690.

(13)   Sum, T. C.; Mathews, N. *Energy & Environmental Science* **2014**, *7*, 2518.

(14)   Smith, I. C.; Hoke, E. T.; Solis-Ibarra, D.; McGehee, M. D.; Karunadasa, H. I. *Angewandte Chemie* **2014**, *126*, 11414.

(15)   Zuo, L.; Gu, Z.; Ye, T.; Fu, W.; Wu, G.; Li, H.; Chen, H. *Journal of the American Chemical Society* **2015**, *137*, 2674.

(16)   Ono, L. K.; Raga, S. R.; Wang, S.; Kato, Y.; Qi, Y. *Journal of Materials Chemistry A* **2015**, *3*, 9074.

(17)   Jeon, N. J.; Noh, J. H.; Yang, W. S.; Kim, Y. C.; Ryu, S.; Seo, J.; Seok, S. I. *Nature* **2015**, *517*, 476.

(18)   Green, M. A.; Ho-Baillie, A.; Snaith, H. J. *Nature Photonics* **2014**, *8*, 506.

(19)   Stender, A. S.; Marchuk, K.; Liu, C.; Sander, S.; Meyer, M. W.; Smith, E. A.; Neupane, B.; Wang, G.; Li, J.; Cheng, J.-X.; Huang, B.; Fang, N. *Chemical Reviews* **2013**, *113*, 2469.

(20)   Stranks, S. D.; Eperon, G. E.; Grancini, G.; Menelaou, C.; Alcocer, M. J. P.; Leijtens, T.; Herz, L. M.; Petrozza, A.; Snaith, H. J. *Science* **2013**, *342*, 341.

(21)   Dong, Q.; Fang, Y.; Shao, Y.; Mulligan, P.; Qiu, J.; Cao, L.; Huang, J. *Science* **2015**, *347*, 967.

(22)   Wehrenfennig, C.; Liu, M.; Snaith, H. J.; Johnston, M. B.; Herz, L. M. *Energy & Environmental Science* **2014**, *7*, 2269.

(23)   Xing, G.; Mathews, N.; Sun, S.; Lim, S. S.; Lam, Y. M.; Grätzel, M.; Mhaisalkar, S.; Sum, T. C. *Science* **2013**, *342*, 344.

(24)   Fu, Y.; Meng, F.; Rowley, M. B.; Thompson, B. J.; Shearer, M. J.; Ma, D.; Hamers, R. J.; Wright, J. C.; Jin, S. *Journal of the American Chemical Society* **2015**, *137*, 5810.

(25)   Li, G.; Tan, Z.-K.; Di, D.; Lai, M. L.; Jiang, L.; Lim, J. H.-W.; Friend, R. H.; Greenham, N. C. *Nano Letters* **2015**, *15*, 2640.

(26)   Zhu, H.; Fu, Y.; Meng, F.; Wu, X.; Gong, Z.; Ding, Q.; Gustafsson, M.; Trinh, M.; Jin, S.; Zhu, X. *Nature Materials* **2015**, *14*, 636.

(27)   Berhe, T. A.; Su, W.-N.; Chen, C.-H.; Pan, C.-J.; Cheng, J.-H.; Chen, H.-M.; Tsai, M.-C.; Chen, L.-Y.; Dubale, A. A.; Hwang, B.-J. *Energy & Environmental Science* **2016**, *9*, 323.

(28)   Niu, G.; Guo, X.; Wang, L. *Journal of Materials Chemistry A* **2015**, *3*, 8970.

(29)   Ito, S.; Tanaka, S.; Manabe, K.; Nishino, H. *The Journal of Physical Chemistry C* **2014**, *118*, 16995.

(30)   Hoke, E. T.; Slotcavage, D. J.; Dohner, E. R.; Bowring, A. R.; Karunadasa, H. I.; McGehee, M. D. *Chemical Science* **2015**, *6*, 613.

(31)   Matsumoto, F.; Vorpahl, S. M.; Banks, J. Q.; Sengupta, E.; Ginger, D. S. *The Journal of Physical Chemistry C* **2015**, *119*, 20810.

(32)   Manshor, N. A.; Wali, Q.; Wong, K. K.; Muzakir, S. K.; Fakharuddin, A.; Schmidt-Mende, L.; Jose, R. *Physical Chemistry Chemical Physics* **2016**, *18*, 21629.

(33)   Aristidou, N.; Sanchez-Molina, I.; Chotchuangchutchaval, T.; Brown, M.; Martinez, L.; Rath, T.; Haque, S. A. *Angewandte Chemie International Edition* **2015**, *54*, 8208.

(34)   Barnes, M. D.; Mehta, A.; Thundat, T.; Bhargava, R. N.; Chhabra, V.; Kulkarni, B. *The Journal of Physical Chemistry B* **2000**, *104*, 6099.

(35)   Glennon, J. J.; Buhro, W. E.; Loomis, R. A. *The Journal of Physical Chemistry C* **2008**, *112*, 4813.

(36)   Glennon, J. J.; Tang, R.; Buhro, W. E.; Loomis, R. A. *Nano letters* **2007**, *7*, 3290.

(37)   Kuno, M.; Fromm, D. P.; Gallagher, A.; Nesbitt, D. J.; Micic, O. I.; Nozik, A. J. *Nano Letters* **2001**, *1*, 557.

(38)   Kuno, M.; Fromm, D. P.; Hamann, H. F.; Gallagher, A.; Nesbitt, D. J. *The Journal of Chemical Physics* **2001**, *115*, 1028.

(39)   Kuno, M.; Fromm, D. P.; Hamann, H. F.; Gallagher, A.; Nesbitt, D. J. *The Journal of Chemical Physics* **2000**, *112*, 3117.

(40)   Galland, C.; Ghosh, Y.; Steinbrück, A.; Sykora, M.; Hollingsworth, J. A.; Klimov, V. I.; Htoon, H. *Nature* **2011**, *479*, 203.

(41)   Tian, Y.; Merdasa, A.; Peter, M.; Abdellah, M.; Zheng, K.; Ponseca, C. S.; Pullerits, T.; Yartsev, A.; Sundström, V.; Scheblykin, I. G. *Nano Letters* **2015**, *15*, 1603.

(42)   Wen, X.; Ho-Baillie, A.; Huang, S.; Sheng, R.; Chen, S.; Ko, H.-c.; Green, M. A. *Nano Letters* **2015**, *15*, 4644.

(43)   Park, Y.-S.; Guo, S.; Makarov, N. S.; Klimov, V. I. *ACS Nano* **2015**, *9*, 10386.

(44)   Seth, S.; Mondal, N.; Patra, S.; Samanta, A. *The Journal of Physical Chemistry Letters* **2016**, *7*, 266.

(45)   Zhu, F.; Men, L.; Guo, Y.; Zhu, Q.; Bhattacharjee, U.; Goodwin, P. M.; Petrich, J. W.; Smith, E. A.; Vela, J. *ACS Nano* **2015**, *9*, 2948.

(46)   Tachikawa, T.; Karimata, I.; Kobori, Y. *The Journal of Physical Chemistry Letters* **2015**, *6*, 3195.

(47)   Lidke, K. A.; Rieger, B.; Jovin, T. M.; Heintzmann, R. *Opt. Express* **2005**, *13*, 7052.

(48)   Banin, U.; Bruchez, M.; Alivisatos, A. P.; Ha, T.; Weiss, S.; Chemla, D. S. *The Journal of Chemical Physics* **1999**, *110*, 1195.

(49)   Protesescu, L.; Yakunin, S.; Bodnarchuk, M. I.; Krieg, F.; Caputo, R.; Hendon, C. H.; Yang, R. X.; Walsh, A.; Kovalenko, M. V. *Nano Letters* **2015**, *15*, 3692.

(50)   Bekenstein, Y.; Koscher, B. A.; Eaton, S. W.; Yang, P.; Alivisatos, A. P. *Journal of the American Chemical Society* **2015**, *137*, 16008.

(51)   Akkerman, Q. A.; D'Innocenzo, V.; Accornero, S.; Scarpellini, A.; Petrozza, A.; Prato, M.; Manna, L. *Journal of the American Chemical Society* **2015**, *137*, 10276.

(52)   Jang, D. M.; Park, K.; Kim, D. H.; Park, J.; Shojaei, F.; Kang, H. S.; Ahn, J.-P.; Lee, J. W.; Song, J. K. *Nano Letters* **2015**, *15*, 5191.

(53)   Men, L.; Freppon, D. J.; Bhattacharjee, U.; Zhu, F.; Rosales, B. A.; Petrich, J. W.; Smith, E. A.; Vela, J.

(54)   Zhang, F.; Zhong, H.; Chen, C.; Wu, X.-g.; Hu, X.; Huang, H.; Han, J.; Zou, B.; Dong, Y. *ACS Nano* **2015**, *9*, 4533.

(55)   Pathak, S.; Sakai, N.; Wisnivesky Rocca Rivarola, F.; Stranks, S. D.; Liu, J.; Eperon, G. E.; Ducati, C.; Wojciechowski, K.; Griffiths, J. T.; Haghighirad, A. A.; Pellaroque, A.; Friend, R. H.; Snaith, H. J. *Chemistry of Materials* **2015**, *27*, 8066.

(56)   Yuan, H.; Debroye, E.; Janssen, K.; Naiki, H.; Steuwe, C.; Lu, G.; Moris, M. l.; Orgiu, E.; Uji-i, H.; De Schryver, F. *The Journal of Physical Chemistry Letters* **2016**, *7*, 561.

(57)   Wu, X.; Trinh, M. T.; Niesner, D.; Zhu, H.; Norman, Z.; Owen, J. S.; Yaffe, O.; Kudisch, B. J.; Zhu, X.-Y. *Journal of the American Chemical Society* **2015**, *137*, 2089.

(58)   Duan, H.-S.; Zhou, H.; Chen, Q.; Sun, P.; Luo, S.; Song, T.-B.; Bob, B.; Yang, Y. *Physical Chemistry Chemical Physics* **2015**, *17*, 112.

(59)   Zheng, K.; Zidek, K.; Abdellah, M.; Messing, M. E.; Al-Marri, M. J.; Pullerits, T. *The Journal of Physical Chemistry C* **2016**, *120*, 3077.

(60)   Tian, Y.; Merdasa, A.; Unger, E.; Abdellah, M.; Zheng, K.; McKibbin, S.; Mikkelsen, A.; Pullerits, T.; Yartsev, A.; Sundström, V.; Scheblykin, I. G. *The Journal of Physical Chemistry Letters* **2015**, *6*, 4171.

(61)   Grabolle, M.; Spieles, M.; Lesnyak, V.; Gaponik, N.; Eychmüller, A.; Resch-Genger, U. *Analytical Chemistry* **2009**, *81*, 6285.

(62)   Noh, J. H.; Im, S. H.; Heo, J. H.; Mandal, T. N.; Seok, S. I. *Nano Letters* **2013**, *13*, 1764.

(63)   Buin, A.; Comin, R.; Xu, J.; Ip, A. H.; Sargent, E. H. *Chemistry of Materials* **2015**, *27*, 4405.

(64)   Osborne, M.; Fisher, A. *Nanoscale* **2016**, *8*, 9272.

(65)   Lesoine, M. D.; Bhattacharjee, U.; Guo, Y.; Vela, J.; Petrich, J. W.; Smith, E. A. *The Journal of Physical Chemistry C* **2013**, *117*, 3662.

(66)   Malko, A. V.; Park, Y.-S.; Sampat, S.; Galland, C.; Vela, J.; Chen, Y.; Hollingsworth, J. A.; Klimov, V. I.; Htoon, H. *Nano Letters* **2011**, *11*, 5213.

(67)   deQuilettes, D. W.; Zhang, W.; Burlakov, V. M.; Graham, D. J.; Leijtens, T.; Osherov, A.; Bulovic, V.; Snaith, H. J.; Ginger, D. S.; Stranks, S. D. *Nat Commun* **2016**, *7*, 1.

(68)   van Sark, W. G. J. H. M.; Frederix, P. L. T. M.; Van den Heuvel, D. J.; Gerritsen, H. C.; Bol, A. A.; van Lingen, J. N. J.; de Mello Donegá, C.; Meijerink, A. *The Journal of Physical Chemistry B* **2001**, *105*, 8281.

(69)   Fang, H. H.; Raissa, R.; Abdu-Aguye, M.; Adjokatse, S.; Blake, G. R.; Even, J.; Loi, M. A. *Advanced Functional Materials* **2015**, *25*, 2378.

(70)   Luo, B.; Pu, Y.-C.; Yang, Y.; Lindley, S. A.; Abdelmageed, G.; Ashry, H.; Li, Y.; Li, X.; Zhang, J. Z. *The Journal of Physical Chemistry C* **2015**, *119*, 26672.

CHAPTER 4. PHOTOINDUCED TRANS-TO-CIS PHASE TRANSITION OF POLYCRYSTALLINE AZOBENZENE AT LOW IRRADIANCE OCCURS IN THE SOLID STATE

Ujjal Bhattacharjee[‡], Daniel Freppon[‡], Long Men[‡], Javier Vela, Emily A. Smith,

and Jacob W. Petrich[*]

[‡] Joint co-authors, contributed equally to the work.

[*]Email: jwp@iastate.edu

Abstract

The ability to produce large-scale, reversible structural changes in a variety of materials by photoexcitation of a wide variety of azobenzene derivatives has been recognized for almost two decades. Because photoexcitation of *trans*-azobenzene produces the *cis* isomer in solution, it has generally been inferred that the macroscopic structural changes occurring in materials are also initiated by a similar large-amplitude, *trans*-to-*cis* isomerization. This work provides the first demonstration that a *trans*-to-*cis* photoisomerization occurs in polycrystalline azobenzene (not a derivative) and is consistent with the previously suggested nature of the trigger in the photo actuated mechanisms of the materials in question.   It is also demonstrated that the transition occurs in the solid phase (not *via* a pre-melted phase): under low irradiance, *trans*-to-*cis* isomerization occurs in the solid; and the presence of the *cis*-isomer thus lowers the melting point of the sample, providing a liquid phase. A variety of experimental techniques were employed, including X-ray diffraction measurements of polycrystalline azobenzene during exposure to laser irradiation and fluorescence measurements of the solid sample. (Given the

difficulty of obtaining fluorescence spectra of azobenzene owing to the extremely low quantum yield, 10^{-6} to 10^{-7}, our spectra represent one example of only a handful of fluorescence measurements of azobenzene and, to our knowledge, the first fluorescence spectra of the solid or melted solid.) A practical consequence of this work is that it establishes *trans*-azobenzene as an easily obtainable and well-defined control for monitoring photoinduced structural changes in X-ray diffraction experiments, using easily accessible laser wavelengths.

4.1 Introduction

Photoinduced *trans*-to-*cis* isomerization has been an area of interest for decades not only because of its intrinsic importance as a fundamentally basic process in chemistry and biology but also for its utility in testing various theories of reaction dynamics. More recently, such changes have been implicated in providing photoinduced mechanical transformations important for applications in nanotechnology. The structure of azobenzene is related to that of stilbene (Scheme 1), which is one of the simplest and most studied examples of a system that undergoes an excited-state *trans*-to-*cis* isomerization. Stilbene has been used in studies as diverse as modeling the isomerization in bacteriorhodopsin to testing the role of solvent friction in Kramers' theory of barrier crossing.[1-4] Azobenzene (Scheme 1) is a nitrogen-substituted analog of stilbene that also undergoes excited-state *trans*-to-*cis* isomerization, as was originally noted by Hartley.[5,6] It has been the object of several fundamental photophysical studies and reviews.[7-11]

Stilbene

trans   cis

Azobenzene

trans   cis
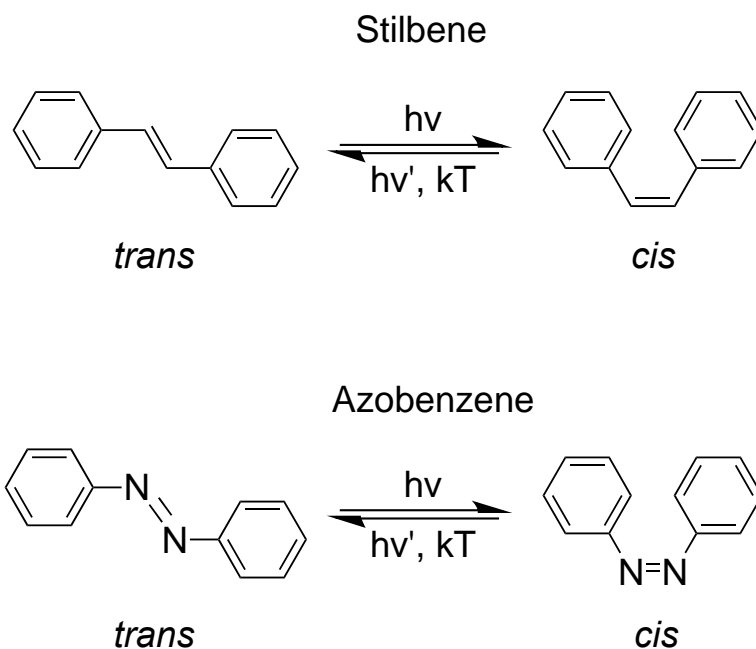
Scheme 4.1. Structures of stilbene and azobenzene, both of which exhibit photoexcited *trans*-to-*cis* isomerization. In both cases, the *cis* form can return to the initial *trans* form either thermally or by photoexcitation. The melting points of *trans*- and *cis*-stilbene are 125 °C and -5 °C,[12] respectively; of *trans*- and *cis*-azobenzene, 68 °C and 71 °C, respectively.[13,14]

More importantly for the purposes of this work are the observations that azobenzene derivatives can be used as a photo actuated switches and the proposals for their applications in nanoscale devices.[15-25] Natanshon *et al*.[20,21] showed that polymers containing azobenzene derivatives could be used for reversible optical storage. Koshima *et al*. observed controlled and reversible mechanical motion of polycrystalline plates of a dimethyl amino derivative of *trans*-azobenzene upon photoexcitation.[26] Most recently, Bushuyev *et al*.[27] extended the studies of Koshima *et al*.[26] to single-crystal "needles" of fluorinated *cis*-azobenzenes. In all these cases, it has been convincingly demonstrated that the mechanical motion of the films, plates, or needles has its origin in a photoinduced structural change of the azobenzene derivative.[15,17-33] In order, however, fully to appreciate and to exploit this fascinating phenomenon of light-induced mechanical motion, it is necessary to understand clearly what the transition is and how it occurs

in situ, more specifically: to confirm that the transition is indeed a large-amplitude *trans*-to-*cis* isomerization and not a smaller structural change; and to determine conclusively whether the structural change occurs in the solid or in the liquid phase.

4.2 Experimental

4.2.1 Materials

Trans-azobenzene was purchased from Matheson (96%), and from Sigma-Aldrich (98%). *Trans*-stilbene (96%) was obtained from Sigma-Aldrich. Coumarin 153 was obtained from Exciton.

4.2.2 Melting experiments with low irradiance

Experiments to determine whether polycrystalline *trans*-azobenzene could be melted with low light levels were performed with an LED (Thorlab) providing 470-nm radiation. A thermocouple (Omega Engineering Inc.) in contact with the crystals registered the temperature at which the crystals melted. The power of the LED with monitored with a power meter (Newport Corporation).

4.2.3 *In-situ* powder X-ray diffraction (XRD) experiments under laser irradiation

XRD data were obtained with a Rigaku Ultima IV (40 kV, 44 mA, The Woodlands, TX) diffractometer using Cu-Kα radiation and a scan speed of 2 degree/min. A metal plate was substituted for the lead glass at the front of the instrument. A hole was cut at the center of the plate to enable laser irradiation of the sample. Samples were ground to a fine powder in an agate mortar and transferred onto a "background-free" quartz sample holder. While collecting XRD data, the samples were excited with 532-nm or 355-nm pulses from a Nd-YAG laser (20 Hz, 5 ns; Surelite II, Continuum, San Jose, CA). At the sample, the laser beam was an ellipse with minor and major axes of 9 and 13 mm (*i.e.*, having an area of 92 mm^2). The irradiances were 8.5

$\times$ 10^5 W/cm^2 and 1.4 $\times$ 10^5 W/cm^2, respectively. These values represent the pulse energy divided by the temporal duration of the pulse divided by the beam area at the sample. These irradiances are orders of magnitude larger than those required to melt trans-azobenzene with 470-nm radiation. This is in part owing to the smaller extinction coefficient at 532 nm with respect that at 470 nm (Fig. 4.1); but it also likely reflects the sensitivity of the X-ray experiment.
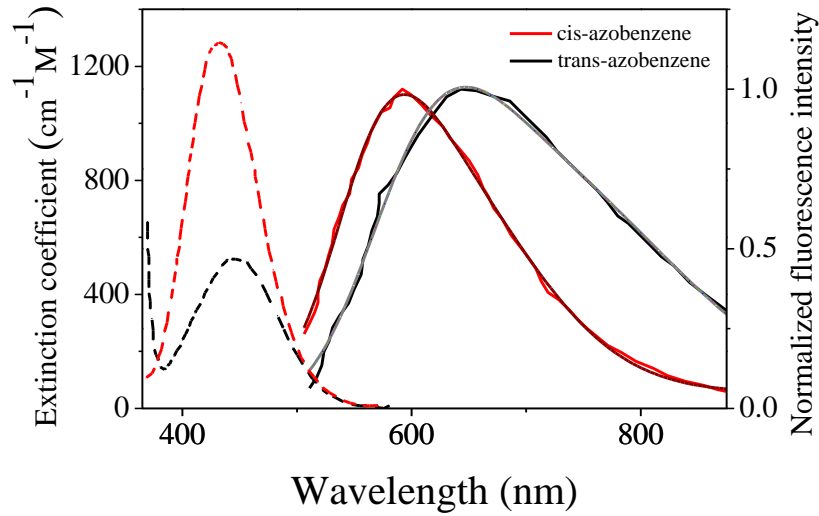
Figure 4.1. Steady-state absorption (dashed lines) and emission (solid lines) spectra of *trans*-(black) and *cis*-azobenzene (red), obtained from a 43-mM sample in DMSO, reproduced from the work of Satzger *et al*.[7] Satzger *et al*. extracted the spectrum of the *cis*-isomer from experimental data containing a mixture of 30% *cis*- and 70% and *trans*-isomers. The spectra are each fit to a sum of lognormals:

$$I_{trans}(\lambda) = \frac{0.35}{0.10\sqrt{2\pi}\lambda} e^{-\frac{\left(ln\frac{\lambda}{623\,nm}\right)^2}{2(0.10)^2}} + \frac{0.65}{0.14\sqrt{2\pi}\lambda} e^{-\frac{\left(ln\frac{\lambda}{745\,nm}\right)^2}{2(0.14)^2}}$$

$$I_{cis}(\lambda) = \frac{0.64}{0.11\sqrt{2\pi}\lambda} e^{-\frac{\left(ln\frac{\lambda}{648\,nm}\right)^2}{2(0.11)^2}} + \frac{0.36}{0.07\sqrt{2\pi}\lambda} e^{-\frac{\left(ln\frac{\lambda}{577\,nm}\right)^2}{2(0.07)^2}}$$

4.2.4 Fluorescence spectra of polycrystalline *trans*-azobenzene

Two types of fluorescence experiments were performed. In both types of experiments, irradiances significantly in excess of that required to observe melting in the sample were required

in order to obtain an observable signal. The irradiances chosen for the fluorescence experiments were based on those required to observe significant structural changes in the X-ray experiments. In the first type of fluorescence experiment, *trans*-azobenzene was melted and allowed to solidify on a glass slide to form a thick film (~1 mm). The sample was excited (λ_{ex} = 532 nm or 355 nm) in a front-faced orientation by the same Nd-YAG laser that was used for the XRD measurements with the same beam area. Fluorescence was collected by a CCD (I-Star, Andor Technology, Belfast, UK) camera fitted with a spectrograph. For clarity, in the course of our discussion, we shall refer to this as the "pulsed, solid film" experiment.

The second type of fluorescence experiment employed a lab-built optical microscope based on a DM IRBE platform (Leica, Wetzlar, Germany) with continuous-wave (cw) laser excitation at 532 nm (Sapphire SF 532 nm, Coherent, Santa Clara, CA, USA). A 10×, 0.25 numerical aperture objective (Leica) was used to achieve a laser spot with a diameter of 2.6 μm. As in the previous experiment, irradiances of ~10^5 W/cm^2 were required. Fluorescence was collected from the *epi*-direction and focused onto a HoloSpec f/1.8i spectrograph (Kaiser Optical Systems, Ann Arbor, MI, USA), equipped with a broad-range grating (HFG-650, Kaiser Optical Systems), and then directed to a CCD (Newton 940, Andor Technology, Belfast, UK). The collection time for a single acquisition was 60 s. This shall be referred to as the "cw, polycrystalline powder" experiment.

4.2.5 Spectral analysis

Satzger *et al.*[34] measured the fluorescence spectra of *trans*- and *cis*-azobenzene in liquid DMSO. We found that each of their fluorescence spectra, reproduced in Fig. 4.1, could be well described by a sum of two lognormal functions. (The lognormal is commonly used to model emission spectra of chromophores in the condensed phase because it adequately represents their

asymmetry.[35]) As will be discussed below, this result motivated us to describe the fluorescence emission of the initially solid samples in terms of lognormals.

4.3 Results

4.3.1 *Trans*-azobenzene melts at low irradiances

Polycrystalline *trans*-azobenzene was subjected to 470-nm radiation from an LED. Melting of the sample began after about 15 s with an irradiance of 240 mW/cm^2, corresponding to a temperature of 50-54 ^{0}C. The sample was predominately melted after 2-3 s with an irradiance of 280 mW/cm^2, corresponding to a temperature of 54-57°C (Movie S4.1), which is lower than the melting point of *trans*-azobenzene (68 $^\circ$C[13,14]). Thus suggests that the photoinduced *trans*-to-*cis* isomerization occurs in the solid phase and that it is followed by melting, as the presence of the newly-formed *cis*-isomer has now depressed the melting point of the sample. The presence of the *cis*-isomer is clearly and reproducibly shown in the absorption spectrum of the material (dissolved in DMSO) before and after irradiation (Fig. 4.2). As a control experiment, similar measurements were performed with coumarin 153 (melting point of 164-168 ^{0}C[36]), which absorbs light strongly at 470 nm ($\varepsilon_{470} = 5000$ M^{-1} cm^{-1} [37]) but does not undergo any significant nonradiative photo processes.[38] The coumarin sample was exposed for up to 2 min to a range of irradiances from 280 to 800 mW/cm^2, over which range no melting was observed, suggesting that a temperature of 164-168 $^\circ$C could not have been achieved in this range of irradiances, which exceeded that used to melt the *trans*-azobenzene.
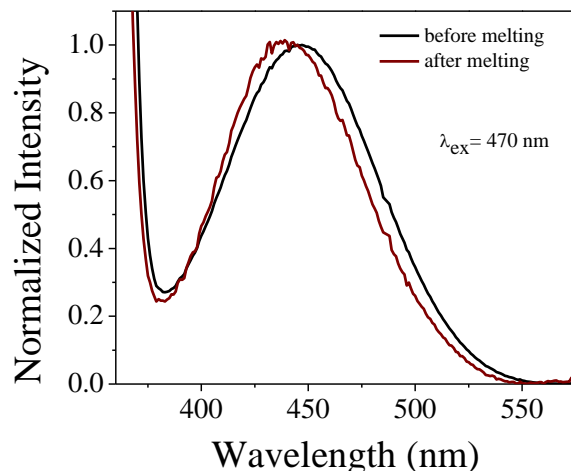
Figure 4.2. Steady-state absorption of a *trans*-azobenzene sample dissolved in DMSO before (black) and after (red) melting, which is effected by 470-nm radiation.

4.3.2 *In-situ* laser-XRD structural analysis

The powder X-ray diffraction (XRD) of *trans*- and *cis*-azobenzene are presented in Fig. 4.3. Before laser irradiation, the experimental pattern of *trans*-azobenzene agrees well with that of the standard. Intensity differences between the two are attributed to preferred orientations within the crystalline solid. With λ_{ex} = 355 nm and an irradiance of 1.4×10^5 W/cm^2, the diffraction peaks at 16.1 and 19.9° (highlighted in green) are significantly enhanced. These two peaks match those of the *cis*-azobenzene standard, suggesting that a significant fraction of the *trans*-azobenzene population photo isomerizes to the *cis* form. On the other hand, the diffraction pattern obtained with λ_{ex} = 532 nm is nearly identical to that of the unilluminated *trans*-azobenzene, except for a peak at 15.9°, which might be attributed to a small amount of *cis*-azobenzene. Owing to the lower absorbance at 532 nm relative to that at 355 nm (~170 times lower, Fig. 4.1), it is not surprising to expect a lower yield of *trans*-to-*cis* conversion with 532-nm excitation. The irradiances employed suggest (as is verified below) that the diffraction pattern is obtained with a sample which has been melted and cooled during the experiment.
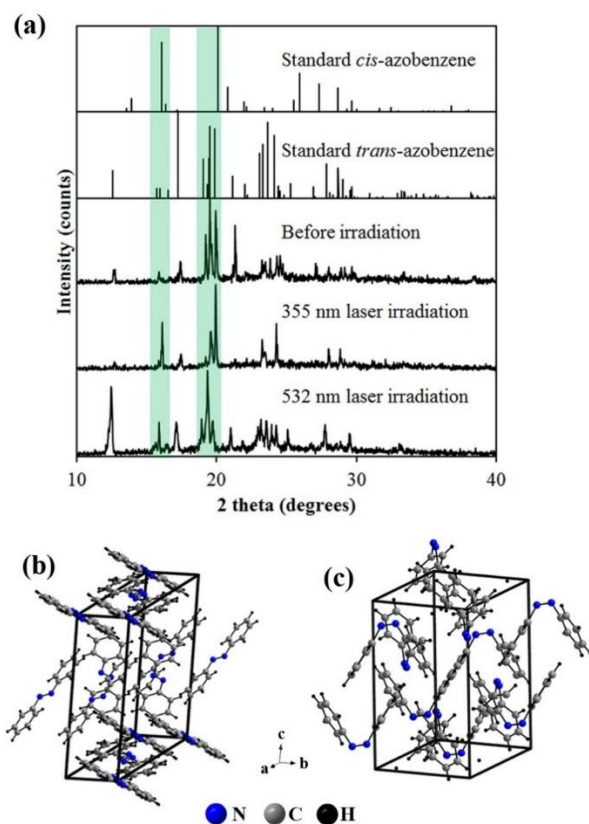
Figure 4.3. (a) Powder X-ray diffraction of *trans*-azobenzene before and upon laser irradiation at 355 nm and 532 nm. The standard patterns for the *trans*- and the *cis*-isomers are from Mostad and Rømming[39] and from Harada and Ogawa,[40] respectively. Crystalline unit cells of (b) *trans*- and (c) *cis*-azobenzene.[39,40] The detection limit of the powder XRD method is estimated to be a few percent.[41]

A similar *in-situ* laser-XRD experiment was also performed on *trans*-stilbene (Fig. 4.4). In this case, however, upon 355-nm laser irradiation (there is no absorption at 532 nm), the characteristic *trans*-pattern diminishes without the appearance of new peaks. These results were interpreted in terms of photoisomerization also occurring in stilbene. The melting point of *cis*-stilbene is -5 °C (compared to 125 °C for the *trans*-form),[12] meaning any *cis* product generated at room temperature in this case would necessarily exist in the liquid phase, which would thus preclude the generation of a diffraction pattern.

68
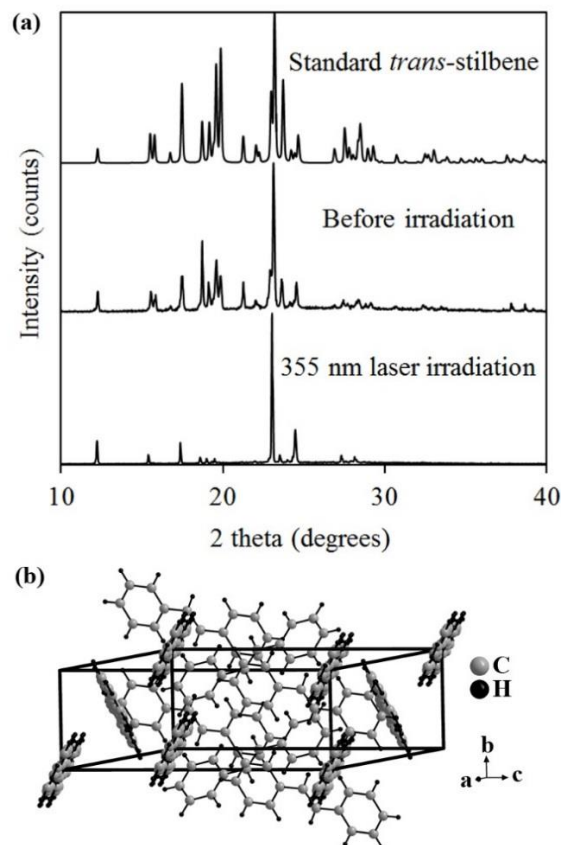
Figure 4.4. (a) Powder X-ray diffraction of *trans*-stilbene before and upon laser irradiation at 355 nm and (b) the unit cell of *trans*-stilbene. A standard pattern of the *cis* isomer could not be found in the literature.

4.3.3 Fluorescence measurements

Few measurements of the fluorescence of azobenzene have previously been collected in solution.[7,42,43] This is because the fluorescence quantum yields of *trans*- and *cis*-azobenzene lie in the range of 10^{-6} to 10^{-7}, and the intensities of their fluorescence spectra in DMSO, for example, are comparable to the Raman peak of DMSO itself. This led Satzger *et al*. to use a modified Raman spectrometer to collect and to construct the *trans*- and *cis*-azobenzene spectra (the fluorescence maxima lie at 630 nm and 570 nm, respectively), which are reproduced in Fig. 4.1. The fluorescence spectrum of the *cis*- isomer is blue-shifted with respect to that of the *trans*-isomer. We fit the spectrum of each isomer to a sum of two lognormal functions (provided

in the caption to Fig. 4.1), and this motivated our choice for modeling the results described

below. The spectrum of solid (or pure liquid) azobenzene is clearly different from those in dilute

solution, as expected given the possible interactions of the chromophores in the pure solid. In

both cases, however, the species attributed to the *cis*-isomer is blue shifted with respect to that of

the *trans*-isomer.

The spectra of the initially solid *trans*-azobenzene samples in *all* of the "pulsed, solid

film" and the "cw, polycrystalline powder" experiments are well described in terms of lognormal

functions, *per* equations 1 and 2:

$$I_{trans}(\lambda) = \frac{0.88}{0.097\sqrt{2\pi}\lambda}e^{-\frac{\left(ln\frac{\lambda}{692\,nm}\right)^2}{2(0.097)^2}} + \frac{0.12}{0.091\sqrt{2\pi}\lambda}e^{-\frac{\left(ln\frac{\lambda}{628\,nm}\right)^2}{2(0.091)^2}} \tag{1}$$

$$I_{cis}(\lambda) = \frac{1}{0.091\sqrt{2\pi}\lambda}e^{-\frac{\left(ln\frac{\lambda}{628\,nm}\right)^2}{2(0.091)^2}} \tag{2}$$

The maximum of equation 1 is at 679 nm and is determined by the weights of the two

components comprising the function (0.88 and 0.12). The maximum of equation 2 is at 624 nm.

It is fortuitous that the characteristic wavelength in the logarithmic argument of the exponent of

I$_{cis}$, 628 nm, matches that of one of the components of *I$_{trans}$*. The fluorescence spectra of the

solid-state samples were then described by a linear combination of these *trans* and *cis* spectra:

$$I(\lambda) = A_t I_{trans}(\lambda) + A_c I_{cis}(\lambda) \tag{3}$$

In fitting the solid-state data, all parameters were kept constant except the weights of the

individual profiles, *A$_t$* and *A$_c$,* as indicated in equation 3. These "global fitting" results are

compiled in Table 4.1, which summarizes the results of the fluorescence experiments.

Table 4.1. Decomposition of the azobenzene fluorescence with a summary of the spectra into that of the t*rans*- and c*is*-Isomers. The spectra are globally fit to equations 1-3: $I(\lambda) = A_t I_{trans}(\lambda) + A_c I_{cis}(\lambda)$. Only the amplitudes, A_t and A_c, are varied. The emission maxima of I_{trans} and I_{cis} are 679 nm and 624 nm, respectively.

Sample	Conditions	A_t	A_c
solid film	pulsed laser, λ_{ex} = 532 nm	0.86	0.14
solid film	pulsed laser, λ_{ex} = 355 nm	0.64	0.36
polycrystalline powder	cw laser, before melting, λ_{ex} = 532 nm	1.00	0.00
polycrystalline powder	cw laser, after melting, λ_{ex} = 532 nm	0.64	0.36

Representative fluorescence spectra obtained from the "pulsed, solid film" experiments are presented in Fig. 4.5. When λ_{ex} = 355 nm, the fluorescence spectrum is broader than that obtained when λ_{ex} = 532 nm; and it is also extended towards the blue. The appearance of new emission in the blue is consistent with the generation of the *cis*-isomer. (It was not possible to obtain a spectrum of the *trans*-isomer, as the laser power required to obtain a spectrum was also able to convert it to the *cis*-isomer.) Owing to the weak optical density of *trans*-azobenzene at 532 nm, it was impossible to produce more than 14% of the *cis*-isomer (Table 4.1) without the high peak power of the pulsed laser inducing sample damage. It is noteworthy that irradiances in excess of 3 x 10^5 W/cm^2 at 532 nm did not provide further spectral changes, and this will be commented on below.
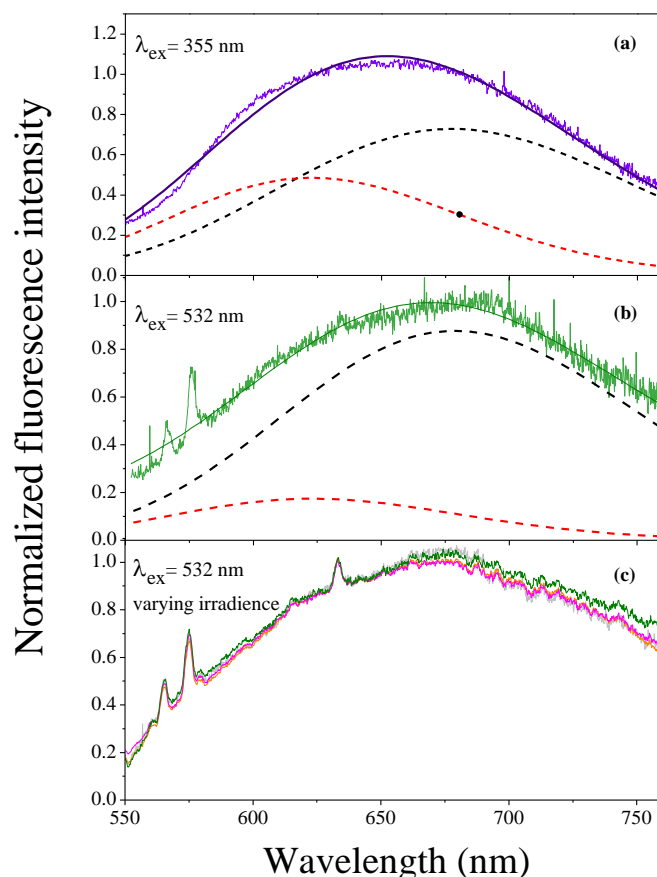
Figure 4.5. Fluorescence spectra of solid azobenzene at two excitation wavelengths and varying irradiances.

a λ_{ex} = 355 nm. Irradiance = 6 x 10^4 W/cm^2.

b λ_{ex} = 532 nm. Irradiance = 1 x 10^5 W/cm^2.

c λ_{ex} = 532 nm.   The values of the irradiance were 3 x 10^5 W/cm^2 (olive), 6 x 10^5 W/cm^2 (magenta), 12 x 10^5 W/cm^2 (orange) and 30 x 10^5 W/cm^2 (gray).

Although all the laser powers used were above that which provided melting in the fluorescence microscopy experiment, there is no change in the spectra with increasing laser power. Spectra were decomposed into two spectra, I_{trans} and I_{cis} (equations 1-3). Only the amplitudes of I_{trans} and I_{cis} vary with λ_{ex}. 355-nm excitation produces a spectrum that is broader than that obtained with λ_{ex} = 532 nm and extended towards bluer wavelengths, which is consistent with the optical density of *trans*-azobenzene being ~170 times greater at 355 nm than at 532 nm. Results are summarized in Table 4.1. Raman peaks are evident in panels b and c.

In the parallel set of "cw, polycrystalline powder" experiments, a fluorescence microscope and a cw laser operating at 532 nm were employed. Because the cw laser could be focused to a spot size of 2.6 μm with the microscope objective, despite the low optical density of azobenzene at 532 nm, sufficiently high irradiances could be obtained to generate greater amounts of the *cis*-isomer than in the pulsed experiment at 532 nm described above. In addition, the microscope furnished the additional benefits of not only enabling the efficient collection of fluorescence spectra of the photoisomerization reaction but also permitting the direct visual observation of the sample (which undergoes melting at these large irradiances). Results are presented in Fig. 4.6 and Table 4.1. Up to an irradiance of 1×10^5 W/cm^2, the spectrum was adequately represented by 100% $I_{trans}(\lambda)$. On the other hand, at irradiances greater than 1×10^5 W/cm^2, the spectrum broadens towards bluer wavelengths; and melting is observed. For example, at 7.6×10^5 W/cm^2 the spectrum is well described by a population of 64% *trans*- and 36% *cis*-isomers. At irradiances greater than 7.6×10^5 W/cm^2, the spectra do not evolve further. (A similar phenomenon was observed with our experiments for solid films, where no spectral changes were observed beyond 3×10^5 W/cm^2.) That the spectral changes in both the "pulsed, solid film" and the "cw, polycrystalline powder" experiments reach a plateau at a certain irradiance is most likely because at a given irradiance the melted and isomerized azobenzene "spills" out of the region being interrogated and hence cannot be detected. As noted above in the context of the X-ray experiments, 532 nm is not an optimum wavelength at which to perform these experiments. The high irradiances required reflect can be attributed to the low extinction coefficient and the exceptionally low fluorescence quantum yields of the two isomers.

4.4 Discussion

There is a rich literature treating both the photoinduced properties of azobenzenes in solution[7-11] as well as in polymer films and liquid crystals (see the following citations and references contained within).[15,17-25,28-33] Much less work has been performed on pure solids.[26,27] The work on polymer films and liquid crystals provides convincing evidence that illumination of azobenzene derivatives generates significant macroscopic structural changes to the material and that these structural changes are correlated with large-scale structural changes of the azobenzene derivatives. For example, applying a rotational diffusion model to polarized absorption spectra of azobenzene-containing polyglutamate films, Sekkat *et al.*[44] used the absorption anisotropies at 360 and 420 nm (measuring the *trans* form and photoproduct, respectively). That is, at various times, they measured $[A(\lambda) – A(\lambda)]/[A(\lambda) + 2A(\lambda)]$, where $\lambda = 360$ nm or 420 nm. The anisotropy is related to the second Legendre polynomial and, hence, to the order parameter.[32] From these data, it was determined that the transition dipole moment of the photoproduct was, on average, at about 57° with respect to that of the initially excited trans species. Karageogiev *et al.*[45] argued that the optically-induced mechanical manipulation of azopolymers was a result of local softening of a region of the polymer, rendering it fluid, while the rest of the matrix remains rigid.

Our experiments are most nearly related to those of Koshima *et al.*[26] and Bushuyev et al.[27] , who studied *pure solid samples*: polycrystalline plates of *trans*-azobenzene and single-crystal needles of fluorinated *cis*-azobenzene, respectively. In each case, light-induced, reversible, macroscopic structural changes of the solids are observed and it is suggested that the structural changes are triggered by large-amplitude isomerization. The results, while consistent

with structural change in the material are not, however, compelling evidence that a *trans*-to-*cis* isomerization occurs.

For example, Koshima *et al.*[26] investigated $525 \times 280 \times 5$-μm^3 polycrystalline plates of a dimethyl amino azobenzene. They cite optical absorption spectra, NMR spectra, and X-ray data to document structural changes after illumination. These measurements all provided evidence that changes are induced in the material upon illumination; but they were only suggestive of photoinduced *trans*-to-*cis* isomerization. Namely, in the region of 350 nm to 600 nm, slight changes to the shape of the absorption spectra of the plates are observed after 30 seconds of 365-nm irradiation at 5 mW/cm^2. Also, absorption of the plates dissolved in benzene decreases in this spectral region after illumination. The work of Satzger *et al.*, however, indicates that production of the *cis*-isomer should increase the absorption between 350 and 600 nm (Fig. 4.3). In addition, the NMR data of Koshima *et al.*[26] indicate that after illumination the ratio of the *cis*-to *trans*-azobenzene is only 1/160, which seems too small an amount to generate the evident, large-scale structural change they observe in their sample. Finally, their X-ray data, taken over a limited angular range ($5° < 2\theta < 25°$) also indicate only a small reduction of the signatures attributed to the *trans*-species subsequent to illumination.

The X-ray data reported by Bushuyev *et al.*[27] for single-crystal needles (up to 10-20 μm thick) of fluorinated *cis*-azobenzene, on the other hand, show that a negligible amount of *cis*-to-*trans* isomerization has occurred subsequent to illumination. This may partly be attributed to the fluorination of the azobenzene, but it is likely more significant that they start with *cis* single crystals. For example, Fausto and coworkers[46,47] measured and computed the vibrational spectra of *trans*- and *cis*-stilbene in solid argon and xenon matrices at 15 K. They were *unable* to produce a photoinduced *trans*-to-*cis* isomerization but did succeed in generating *trans*-stilbene

from *cis*-stilbene in the matrices. The results of these two groups suggest that generating a genuine *trans*-to-*cis* isomerization in pure solid azobenzene may be unlikely. As early as 1964, Tsuda and Kuratini[48] demonstrated that solid *cis*-azobenzene could be photo isomerized to the *trans* form.

MacGillivray and coworkers,[47] however, have demonstrated a single-crystal to single-crystal photoinduced synthesis of a starting material containing azobenzene in a *trans* conformation. The results present here demonstrate that photoinduced *trans*-to-*cis* isomerization occurs in pure polycrystalline azobenzene.

4.5 Conclusions

It has been convincingly and elegantly demonstrated that polymer films and liquid-crystal polymers containing azobenzene derivatives[26,27,49-52] *all* undergo large-scale, reversible changes that are induced upon excitation of the azobenzene chromophore; and it has very reasonably been inferred that these changes are a result of a large-amplitude trans-to-cis photoisomerization of the azobenzene derivative. Koshima *et al.*[26] and Bushuyev *et al.*[27] address this issue more directly by studying pure solid samples of azobenzene derivatives. The work presented here confirms (by means of X-ray diffraction and fluorescence spectroscopy) that the photoinduced structural change in *trans*-azobenzene itself is an isomerization to the *cis*-form. It also demonstrates, consistent with the observations of MacGillivray and coworkers,[47] that the isomerization occurs *via* the solid phase.   For pure polycrystalline trans-azobenzene, we have shown that this occurs at 280 mW/cm^2, in agreement with the similar studies on related samples by Koshima *et al.*[26] and Bushuyev *et al.*[27] Furthermore and, perhaps most importantly, our results clearly indicate that subsequent to isomerization of the solid at this low irradiance, the sample melts. We suggest that the fluidity afforded by this sample-induced melting is very likely a crucial aspect of the

mechanical changes that have been the object of such intense investigation over the years. Finally, a very practical result of this work is that it demonstrates that *trans*-azobenzene can be used as easily obtainable and well-defined control for monitoring photoinduced structural changes in X-ray diffraction experiments.

4.6 Acknowledgements

Chapter 3 Supplementary Information

Methods

Melting experiments with low irradiance. Polycrystalline *trans*-azobenzene was subjected to 470-nm radiation (LED, Thorlab). The crystals start to melt at an irradiance of 240 mW/cm^2. A thermocouple was placed in contact with the crystals during the transformation and registered a temperature of 50-54 ^{0}C (the melting begins after ~30 s of exposure). Melting was more pronounced with an irradiance of 280 mW/cm^2 (melting starts "instantaneously"), which provided a more facile measurement since during melting the thermocouple tip was covered with molten material. Here, the temperature was found to be 54-57 ^{0}C. In both instances, these temperatures are lower than that of the melting point of pure *trans*-azobenzene (68 °C). This suggests that a *trans*-to-*cis* isomerization occurs in the solid and that the presence of the newly-formed *cis*-isomer depresses the melting point of the sample. As a control experiment, coumarin 153 (m.p. of 164-168 ^{0}C) was subjected to a range of irradiances from 280 mW/cm^2 to 800

mW/cm², over which no melting was observed for an exposure time of 2 min in each case. At the maximum irradiance, a temperature of 70-75 ^{0}C, slightly in excess of the melting point of *trans*-azobenzene. It is likely that the temperature of the sample is higher because in the absence of melting optimum thermal contact between the sample and the thermocouple cannot be achieved. (The surface of the coumarin crystals blackens at the maximum irradiance, possibly as a result of photo degeneration of dye).
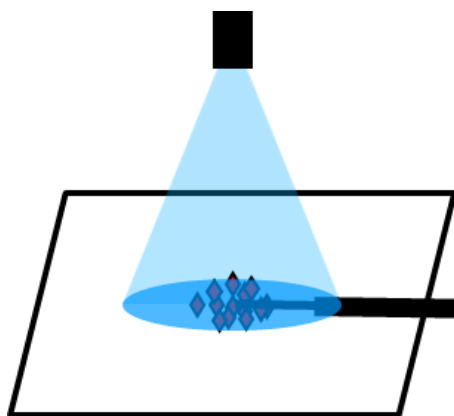

Figure S4.1. LED light illuminates the crystals. During melting, the temperature is measured with a thermocouple.

Movie S4.1. *Trans*-azobenzene subjected to 470-nm illumination at irradiances of 200 mW/cm² and 240 mW/cm². The movie shows melting and movement of the azobenzene crystals in the illumination are beginning at an irradiance of 240 mW/cm². The surface area of the crystal was approximately 0.25 mm².

Movie S4.2. Coumarin 153 subjected to 470-nm illumination at irradiances of 600 mW/cm² and 800 mW/cm². Coumarin 153 does not melt even at the maximum intensity for a 2-min exposure. The crystal surface area was approximately 0.3 mm²

References

(1)   Waldeck, D. H. *Chem. Rev.* **1991**, *91*, 415.

(2)   Nojima, H.; Saito, M.; Inagaki, M. *Rev. Phys. Chem. Jpn.* **1976**, *46*.

(3)   Fleming, G. R. *Chemical Applications of Ultrafast Spectroscopy*; University Press: Oxford, London, 1986.

(4)   Haran, G.; Wynne, K.; Xie, A.; He, Q.; Chance, M.; Hochstrasser, R. M. *Chem. Phys. Lett* **1996**, *261*, 389.

(5)   Hartley, G. *Nature* **1937**, *140*, 281.

(6)   Hartley, G. S. *Journal of the Chemical Society (Resumed)* **1938**, 633.

(7)   Satzger, H.; Spörlein, S.; Root, C.; Wachtveitl, J.; Zinth, W.; Gilch, P. *Chem. Phys. Lett* **2003**, *372*, 216.

(8)   Nagele, T.; Hoche, R.; Zinth, W.; Wachtveitl, J. *Chem. Phys. Lett* **1997**, *272*, 489.

(9)   Mayer, S. T.; Thomsen, C. L.; Philpott, M. P.; Reid, P. J. *Chem. Phys. Lett* **1999**, *314*, 246.

(10)   Tamai, N.; Miyasaka, H. *Chem. Rev.* **2000**, *100*, 1875.

(11)   Rau, H. In *Photochemistry and Photophysics*; Rabek, J. F., Ed.; CRC Press, Inc.: Boca Raton, Florida, 1990; Vol. 2, p 119.

(12)   Weast, R. C.; Astle, M. J.; Beyer, W. H. *CRC Handbook of Chemistry and Physics*; 96th ed. ed.; CRC Press: Boca Raton, FL, 2015.

(13)   Hartley, G. S. *Nature* **1937**, 281.

(14)   Hartley, G. S. *J. Chem. Soc.* **1938**, 633.

(15)   Saha, S.; Stoddart, J. F. *Chem. Soc. Rev.* **2007**, *36*, 77.

(16)   Bandara, H. M. D.; Burdette, S. C. *Chem. Soc. Rev.* **2012**, *41*, 1809.

(17)   Priimagi, A.; Saccone, M.; Cavallo, G.; Shishido, A.; Pilati, T.; Metrangolo, P.; Resnati, G. *Adv. Mater.* **2012**, *24*, OP345.

(18)   Yu, H.; Ikeda, T. *Adv. Mater.* **2011**, *23*, 2149.

(19)   Merino, E.; Ribagorda, M. *Beilstein J. Org. Chem.* **2012**, *8*, 1071.

(20)   Natansohn, A.; Rochon, P. *Chem. Rev.* **2002**, *102*, 4139.

(21)   Natansohn, A.; Rochon, P.; Gosselin, J.; Xie, S. *Macromolecules* **1992**, *25*, 2268.

(22)   Hogan, P. M.; Tajbakhsh, A. R.; Terentjev, E. M. *Phys. Rev. E* **2002**, *65*, 041720.

(23)   El Halabieh, R. H.; Mermut, O.; Barrett, C. J. *Pure Appl. Chem.* **2004**, *76*, 1445.

(24)   Mamiya, J.-I. *Polymer J.* **2013**, *45*, 239.

(25)   Lee, S.; Kang, H. S.; Park, J.-K. *Adv. Mater.* **2012**, *24*, 2069.

(26)   Koshima, H.; Ojima, N.; Uchimoto, H. *J. Am. Chem. Soc.* **2009**, *131*, 6890.

(27)   Bushuyev, O. S.; Tomberg, A.; Friščić, T.; Barrett, C. J. *J. Am. Chem. Soc.* **2013**, *135*, 12556.

(28)   Kamenjicki, M.; Lednev, I. K.; Asher, S. A. *J. Phys. Chem. B* **2004**, *108*, 12637.

(29)   Kamenjicki, M.; Lednev, I. K.; Mikhonin, A.; Kesavamoorthy, R.; Asher, S. A. *Adv. Funct. Mater.* **2003**, *13*, 774.

(30)   Bandara, H. M. D.; Burdette, S. C. *Chem. Soc. Rev.* **2012**, *41*, 1809.

(31)   Azuma, J.; Tamai, N.; Shishido, A.; Ikeda, T. *Chem. Phys. Lett* **1998**, *288*, 77.

(32)   Fujii, T.; Kuwahara, S.; Katayama, K.; Takado, K.; Ubeb, T.; Ikeda, T. *Phys.Chem.Chem.Phys.* **2014**, *16*, 10485.

(33)   Yu, Y.; Nakano, M.; Shishido, A.; Shiono, T.; Ikeda, T. *Chem. Mater.* **2004**, *16*, 1637.

(34)   Satzger, H.; Spörlein, S.; Root, C.; Wachtveitl, J.; Zinth, W.; Gilch, P. *Chemical Physics Letters* **2003**, *372*, 216.

(35)   Fee, R. S.; Maroncelli, M. *J. Chem. Phys.* **1994**, *183*, 235.

(36)   5.4 ed.; Sigma-Aldrich Corporation: Saint Louis, MO, 2014.

(37)   Mühlpfordt, A.; Schanz, R.; Ernsting, N. P.; Farztdinov, V.; Grimme, S. *Phys Chem Chem Phys* **1999**, *1*, 3209.

(38)   Chowdhury, P. K.; Halder, M.; Sanders, L.; Anderson, J. L.; Armstrong, D. W.; Song, X.; Petrich, J. W. *J. Phys. Chem. B* **2004**, *108*, 10245.

(39)   Rømmin, C. *Acta Chem. Scand.* **1971**, *25*, 3561.

(40)   Ogawa, K. *J. Am. Chem. Soc.* **2004**, *126*, 3539.

(41)   Chung, F. H. *J. Appl. Cryst.* **1974**, *7*, 526.

(42)   Fujino, T.; Arzhansev, S. Y.; Tahara, T. *J. Phys. Chem. A* **2001**, *105*, 8123.

(43)   Lu, Y.-C.; Chang, C.-W.; Diau, E. W.-G. *J. Chin. Chem. Soc.* **2002**, *49*, 693.

(44)   Sekkat, Z.; Wood, J.; Knoll, W. *J. Phys. Chem.* **1995**, *99*, 17226.

(45)   Karageorgiev, P.; Neher, D.; Schulz, B.; Stiller, B.; Pietsch, U.; Giersig, M.; Brehmer, L. *Nat. Mater* **2005**, *4*, 699.

(46)   Ünsalan, O.; Kus, N.; Jarmelo, S.; Fausto, R. *Spectrochim. Acta Mol. and Biomol. Spectrosc.* **2015**, *136*, 81.

(47)   Papaefstathiou, G. S.; Zhong, Z.; Geng, L.; MacGillivray, L. R. *J. Am. Chem. Soc.* **2004**, *126*, 9158.

(48)   Tsuda, M.; Kuratani, K. *Bulletin of the Chemical Society of Japan* **1964**, *37*, 1284.

(49)   Uchida, E.; Sakaki, K.; Nakamura, Y.; Azumi, R.; Hirai, Y.; Akiyama, H.; Yoshida, M.; Norikane, Y. *Chemistry – A European Journal* **2013**, *19*, 17391.

(50)   Norikane, Y.; Uchida, E.; Tanaka, S.; Fujiwara, K.; Koyama, E.; Azumi, R.; Akiyama, H.; Kihara, H.; Yoshida, M. *Org. Lett.* **2014**, *16*, 5012−5015.

(51)   Norikane, Y.; Uchida, E.; Tanaka, S.; Fujiwara, K.; Nagai, H.; Akiyama, H. *J. Photopolym. Sci. Technol.* **2016**, *29*, 149.

(52)   Uchida, E.; Azumi, R.; Norikane, Y. *Nat. Commun.* **2015**, *6*, 7310.